COMPUTATION OF MAGNETIC FLUX AND CURRENTS IN A TOKAMAK WITH AN IRON CIRCUIT

J. BLUM
Laboratoire d'Analyse Numérique de Paris VI
4, Place Jussieu, 75230 Paris Cedex 05

R. DEI CAS, J.P. MORERA

ASSOCIATION EURATOM-CEA SUR LA FUSION
Département de Physique du Plasma et de la Fusion Contrôlée
Centre d'Etudes Nucléaires
Boîte Postale n° 6, 92260 FONTENAY-AUX-ROSES (FRANCE)

ABSTRACT

The flux pattern in a Tokamak machine with an iron circuit has been identified by means of 2D magnetostatic codes. The flux map has thus been described by means of a certain number of functions depending on the saturation level of the iron core, on the plasma position, on the current and pressure distribution inside the plasma. This description has been used to simulate the evolution of the currents of the various circuits, the plasma equilibrium and its stability.

1. THE TOKAMAK MACHINE : A TRANSFORMER

The Tokamak, a nested tori machine where the plasma is confined so as to control thermonuclear fusion, can be assimilated to a transformer whose secondary winding is the plasma. In the Tokamak of Fontenay-aux-Roses TFR (Fig. 1), the primary winding is consituted by a set of poloidal coils coupled to the plasma by means of a magnetic circuit, which is made of an iron core and of eight iron limbs. The poloidal coils (Fig. 1 and 2) are either placed near the iron core (inner coils), or close to the external limbs (outer coils) just as the equilibrium windings, that generate the complementary vertical magnetic field necessary for plasma equilibrium. The plasma is confined inside a very thin vacuum vessel and is sometimes surrounded by a copper shell, which maintains the plasma in equilibrium by means of the eddy currents induced in it. In TFR 400 there was a copper shell ; but it is no longer the case in TFR 600[1], so that the equilibrium problem is much more difficult in this machine.

The problem is to simulate the evolution of the currents of the various circuits, the plasma equilibrium and its stability. It is first necessary to know at each instant the flux pattern in the machine.

2. TWO-DIMENSIONAL SIMULATIONS OF THE FLUX PATTERNS IN TFR

We have assumed that the flux configuration is axisymetric, that is to say we represent the set of the eight return limbs by a continous cylindrical iron circuit, whose cross-section is the same as any limb cross-section. The currents in the circuits being given, we want to get a precise map of the fluxes induced by these currents. We have therefore to solve the following Maxwell equations :

$$\begin{cases} \text{rot } \vec{H} = \vec{j} \\ \text{div } \vec{B} = 0 \end{cases} \qquad (1)$$

with $\vec{B} = \mu\,(H^2).\vec{H}$

where the function μ has been experimentally determined.

The poloidal magnetic field $\vec{B}_\theta$ can be conveniently expressed with the help of the flux function ψ :

$$\vec{B}_\theta = \frac{1}{2\pi r}\left[\vec{\text{grad}}\ \psi \times \vec{e}_\varphi\right]$$

in the cylindrical coordinates (r, φ, z) (Fig. 3).
We have then :

$$B_z = \frac{1}{2\pi r}\frac{\partial \psi}{\partial r}$$

$$B_r = -\frac{1}{2\pi r}\frac{\partial \psi}{\partial z}$$

The projection on $\vec{e}_\varphi$ of the equation :

$$\vec{\text{rot}}\left(\frac{\vec{B}}{\mu(H^2)}\right) = \vec{j}$$

leads to the following non-linear elliptic equation :

$$\frac{\partial}{\partial z}\left(\frac{1}{\mu'}\frac{\partial \psi}{\partial z}\right) + \frac{\partial}{\partial r}\left(\frac{1}{\mu'}\frac{\partial \psi}{\partial r}\right) = -2\pi\mu_0 j_\varphi \qquad (2)$$

where $\mu' = r\,\mu_r\,(H^2)$, μ_r being the relative permeability.

In the case of the inner or outer coils, the longitudinal density current j_φ will be taken homogeneous in the whole cross-section of the coil.

In the case of the plasma current density, we are particularly interested in the leakage field generated by the plasma current in its own region. We assume that the plasma cross-section is circular and that its current density depends only on the distance ρ' between the considered point and the centre of the plasma cross-section, for example $j_\varphi = j_0\left(1 - \frac{\rho'^2}{a^2}\right)^q$. In the cylindrical approximation, the mean transverse field in the plasma region would be zero. If we consider toroidal effects, this field will be different from zero, but it is no longer possible to choose any arbitrary profile of current density.

Indeed j_φ must verify the equilibrium law :

$$\vec{\text{grad}}\ p = \vec{j} \times \vec{B} \qquad (3)$$

where p is the plasma pressure.

Assuming that the ratio of the minor radius a of the plasma to the major radius R is small, Shafranov has proved[2] that, in the first order approximation, the magnetic surfaces determined by $\psi = C^{te}$ form a system of nested tori with circular non concentric cross-sections, the center of the magnetic surface of radius ρ is displaced inwards relatively to the magnetic axis (i.e. the magnetic surface with a radius equal to zero) by the distance :

$$\mathfrak{Z}(\rho) = \int_0^\rho \frac{\rho'}{r} \Lambda(\rho')\, d\rho'$$

$$\text{where } \Lambda(\rho') = \frac{8\pi}{B_0^2(\rho')} \left[\bar{p}(\rho') - p(\rho')\right] + \frac{l_i(\rho')}{2} \qquad (4)$$

In this formula $\bar{p}(\rho')$ denotes the mean pressure within a circle of radius ρ', $p(\rho')$ and $B_\theta(\rho')$ the pressure and the poloidal field at the periphery of this circle, and $l_i(\rho')$ the internal inductance per unit length of the part of the plasma within the torus of minor radius ρ' :

$$l_i(\rho') = \frac{\int_0^{\rho'} B_\theta^2(r) r dr}{2\rho'^2 B_\theta^2(\rho')}$$

Then the toroidal correction to the plasma current density can be determined by means of the zero order quantities, in the coordinate system (ρ, θ, φ) centered on the magnetic axis (Fig. 3) :

$$j_\varphi^{(1)}(\rho, \theta) = \cos\theta \left\{ -\frac{\rho}{R} \left[j_\varphi^{(0)}(\rho) + \frac{2}{B_\theta^{(0)}(\rho)} \frac{\delta p^{(0)}}{\delta \rho}(\rho) \right] + \mathfrak{Z}(\rho) \frac{\delta j_\varphi^{(0)}}{\delta \rho}(\rho) \right\} \qquad (5)$$

We notice that this first-order correction has a dipole configuration and will generate in the plasma region a transverse field that has the order of $\frac{a}{R} \times B_\theta(a)$ $\left(B_\theta(a) \simeq \frac{2I_p}{10a}\right)$, like the transverse field generated by $j_\varphi^{(0)}$ and due to toroidicity.

Let us assume that :

$$j_\varphi^{(0)}(\rho) = j_0 \left(1 - \frac{\rho^2}{a^2}\right)^q$$

$$p(\rho) = p_0 \left(1 - \frac{\rho^2}{a^2}\right) \qquad (6)$$

$$\text{Then } \bar{p}(\rho) = p_0 \left(1 - \frac{\rho^2}{2a^2}\right)$$

The peakage of the current density is characterized by q, but can also be determined by $l_i = l_i(a)$.

The poloidal beta is defined as the ratio of the kinetic pressure of the plasma to the poloidal magnetic one :

$$\beta = \frac{8\pi \bar{p}(a)}{B_\theta^2(a)} = \frac{4\pi p_0}{B_\theta^2(a)}$$

Let us consider two typical examples :

a) <u>flat current</u> (q = 0)

$$j_\varphi^{(0)} = j_0$$

then $l_i(\rho) = 0{,}5$

$$\mathfrak{Z}(\rho) = \frac{\rho^2}{2R}(\beta + 0{,}25)$$

$$j_\varphi^{(1)}(\rho, 0) = -\cos 0 \frac{\rho}{R}(1 - 2\beta) j_0$$

The first order correction is null for $\beta = 0{,}5$

b) <u>parabolic current</u> (q = 1) :

$$j_\varphi^{(0)}(\rho) = j_0 \left(1 - \frac{\rho^2}{a^2}\right)$$

Then $l_i = l_i(a) = 11/12$

$$\mathfrak{Z}(a) = \frac{a^2}{R}\left(\frac{\beta}{4} + 0{,}162\right)$$

$$j_\varphi^{(1)}(\rho, \theta) = -\cos\theta\, j_0 \frac{\rho}{R} \left[1 - \beta/2 - 1{,}75X + 1/12\, X/(1 - X) - 1/6 \log(1 - X)\right]$$

with $X = \frac{\rho^2}{2a^2}$

We have also considered the cases where q = 2 ($l_i \simeq 1{,}22$) and q = 3 ($l_i \simeq 1{,}45$).

We have now defined the second member of equation (2) and we are able to see how this equation was numerically solved. We need first to define boundary conditions : we shall take $\psi = 0$ on the limits of our mesh that will be taken sufficiently far from the machine so that we can assimilate them to infinity.

Two codes have been used to solve the elliptic non-linear equation (2) :

. The first one is the code POISSON[3]. It is a finite difference SOR code ; it has already been used for planning Tore II[4].

. The second one is the code MAGNETIX[5]. It is a finite element code where Newton's iterations are used to solve non-linearity. The finite elements are triangles where first order Lagrange interpolation is used. The mesh used by MAGNETIX is made of 1500 knots and 3000 triangles (Fig. 4). The important variations of μ in the iron require such a precise mesh.

The MAGNETIX code has a better convergence in saturated cases than the POISSON one and it is more convenient for elaborate current densities such as those given by (5) and (6).

The mean contributions to the magnetic field of the inner and of the outer currents have been measured on the machine between the points A and B (Fig. 4), for various saturation levels of the iron core. The comparison between measurements and computation is represented on Fig. 5.

Let us notice the importance of the values of the air-gaps : the inner air gap has been taken equal to 3.5 mm and the outer one to 2.5 mm, so as to be as close as possible to the measurements made on the device.

The general agreement between simulation and experiments is about 10 %.

3. THE FLUX MAP IN THE TOKOMAK

Systematic studies have been made with currents in the inner coils, outer coils and plasma separately first and then all together. Two-dimensional simulations of the flux patterns have been obtained for various saturation levels of the iron, various positions of the plasma and different values of β and l_i. The position of the plasma is defined by the quantity Δ by which the center of the plasma is displaced relatively to the center of the vacuum vessel (Fig. 3).

The following results have been obtained :

a) The flux ϕ in the iron core and in the medium plane is given by the value of the function ψ at the point C (Fig. 4) and can be represented by a simple function of a ponderated sum of the Ampere-turns ΣI :

$$\Sigma I = I_o + I_i - K\ I_p \quad \text{with} \quad K = k_o + k_1 \Delta \qquad (7)$$

where I_o and I_i denote the total currents respectively in the outer and inner coils, I_p the total plasma current, whereas $k_o = 1{,}02$ and $k_1 = -\ 0{,}5 \times 10^{-3} cm^{-1}$.

As the plasma current is induced by the primary windings, it is obvious that it is flowing in the opposite direction, whence the sign - in (7). The fact that the plasma is in the medium plane and that the coils are not justify the presence of the ponderating coefficient K in (7), which is the more important as the plasma is closer to the iron core.

The function ϕ versus ΣI is given on Fig. 6. This quantity ϕ will be the key-parameter of the system, describing the saturation level of the iron core.

b) The leakage field between the medium plane and the coils can be expressed quasi-linearly in terms of the currents, with coefficients depending on ϕ and Δ :

$$\begin{aligned} \phi_i &= \psi_D - \psi_C = L_1(\phi)\, I_i + L_2(\phi)\, I_o + L_3(\phi, \Delta)\, I_p \\ \phi_o &= \psi_F - \psi_E = L_4(\phi)\, I_i + L_5(\phi)\, I_o + L_6(\phi, \Delta)\, I_p \end{aligned} \qquad (8)$$

where : $L_3(\phi, \Delta) = L_3^o(\phi) + \Delta \frac{\partial L_3}{\partial \Delta}$

$$L_6(\phi, \Delta) = L_6^o(\phi) + \Delta \frac{\partial L_6}{\partial \Delta}$$

Points C, D, E and F are represented on Fig. 4.

Functions (L_1, L_4), (L_2, L_5) and (L_3, L_6) have been identified by simulations with respectively currents I_i, I_o, I_p alone, and additivity has been verified with a precision of 10 % when all the currents are flowing together. Let us notice that those contributions depend only on ϕ and on ϕ and Δ, for the plasma contribution.
Functions L_1, L_2, L_3^o, L_4, L_5, L_6^o are represented on Fig. 7 whereas $\frac{\partial L_3}{\partial \Delta}$ and $\frac{\partial L_6}{\partial \Delta}$ are independent of ϕ :

$$\frac{\partial L_3}{\partial \Delta} = -\ \frac{\partial L_6}{\partial \Delta} = -\ 0{,}022\ {}^{G}/_{kAt/cm}.$$

c) The mean vertical leakage fields in air and in the medium plane have also been expressed in a quasi-linear form :

$$B_v^{(j)} = b_o^{(j)}(\phi, \Delta)\, I_o + b_i^{(j)}(\phi, \Delta)\, I_i + b_p^{(j)}(\phi, \Delta, \beta, l_i)\, I_p \qquad (9)$$

$j \in \{1, 2, 3\}$; s_1, s_2, s_3, being different surfaces defined in Fig. 4

The index j corresponds to the considered region :

. The first region (j = 1) is taken between C and E (Fig. 4) :

$$B_v^{(1)} = \frac{\psi_E - \psi_C}{s_1}$$

. The second (j = 2) is taken between C and I (center of the plasma) :

$$B_v^{(2)} = \frac{\psi_I - \psi_C}{s_2}$$

. The third one (j = 3) is the plasma region (between G and H) :

$$B_v^{(3)} = \frac{\psi_H - \psi_G}{s_3}$$

The superposition principle, expressed in (9), appears to be true with a precision of 5 % in non-saturated cases and 10 - 20 % in saturated ones. Let us notice that, if there is no iron at all, the plasma contribution $b_p^{(3)} I_p$ is well-known in the first order approximation which is considered here and is the opposite of Shafranov's equilibrium field[2] B_{eq} :

$$B_{eq} = \frac{I_p}{10R}\left(\text{Log}\frac{8R}{a} + \beta + \frac{l_i}{2} - 1.5\right) \qquad (10)$$

To keep this formula which gives the mathematical dependance of B_{eq} on β, l_i and Δ, the quantity $b_p^{(3)} I_p$ has been defined as the attraction of the plasma to the core and is obtained by difference between the average field generated by the plasma in its own region in the presence of the iron and the one that would be obtained without iron that is to say the opposite of B_{eq} :

$$b_p^{(3)} I_p = \frac{\psi_H - \psi_G}{s_3} + B_{eq}$$

(there is no current in the coils in this case).

In this third region, which is very important for plasma equilibrium we have obtained :

$$\begin{aligned} b_o^{(3)}(\phi, \Delta) &= \bar{b}_o^{(3)}(\phi) + \Delta \frac{\partial b_o^{(3)}}{\partial \Delta}(\phi) \\ b_i^{(3)}(\phi, \Delta) &= \bar{b}_i^{(3)}(\phi) + \Delta \frac{\partial b_i^{(3)}}{\partial \Delta}(\phi) \\ b_p^{(3)}(\phi, \Delta, \beta, l_i) &= \bar{b}_p^{(3)}(\phi) + \Delta\left(\frac{\overline{\partial b}^{(3)}}{\partial \Delta p}\right)(\phi) + (k_2\Delta + k_3\beta + k_4) \times (l_i - 0{,}5) \end{aligned} \qquad (11)$$

where $\bar{b}_o^{(3)}$, $\bar{b}_i^{(3)}$, $\bar{b}_p^{(3)}$ are represented on Fig 8 ,

$\frac{\partial b_o^{(3)}}{\partial \Delta}$, $\frac{\partial b_i^{(3)}}{\partial \Delta}$, $\frac{\overline{\partial b}_p^{(3)}}{\partial \Delta}$ on Fig. 9, whereas k_2 =-0,017 G/kAt/cm, k_3 = 1,2 G/kAt and k_4 = 0,75 G/kAt.

Let us notice that, when the plasma current density is flat (l_i = 0,5), $b_p^{(3)}$ does not depend on β, whereas this dependance is the larger as the current density is more peaked ; $b_p^{(3)}$ is very much dependant on the peakage of the plasma current density : for a flat current in a centered plasma (Δ = 0) with β = 0 and in a non saturated case, $b_p^{(3)}$ = 1,4 G/kAt, whereas in the same conditions for a peaked current (l_i = 1,5), we have : $b_p^{(3)}$ = 2,15 G/kAt.

The equilibrium equation of the plasma can now be written :

$$B_v^{(3)}(I, \Delta, \beta, l_i) = B_{eq}(I_p, \Delta, \beta, l_i) \qquad (12)$$

where I is the vector of all the currents.

This equation (12) is equivalent to the fact that $\psi_G = \psi_H$; i . e . the most external magnetic surface of the plasma (supposed to be circular) passes through the points G and H (Fig. 4).

Figures 10 and 11 give examples of such equilibrium configurations in non saturated and saturated cases respectively for a plasma having a parabolic current density (total current 202 KA) and a β value of 0,5. The total currents needed in the inner and outer coils to obtain equilibrium are specified on the Figures.

Figures 12 a, b, c, d show the magnetic surfaces inside the plasma for various values of β and l_i. The inner and outer currents calculated to obtain equilibrium are of course differents in the various cases.

4. APPLICATIONS TO THE SIMULATION OF THE CIRCUITS CURRENTS AND TO THE PROBLEM OF EQUILIBRIUM AND STABILITY OF THE PLASMA

The laws established in § 3 enable us not to solve the 2 D magnetostatic problem at each instant, which would be too onerous, and to simulate the evolution of the currents by a system of ordinary differential equations.

The fluxes which are seen by the inner and outer coils and by the plasma ring can be deduced from ϕ, ϕ_i, ϕ_o, $B_v^{(1)}$ and $B_v^{(2)}$. Indeed each inner coil is submitted to the flux ($\phi + \phi_i$), each outer one to ($\phi + s_1 B_v^{(1)} + \phi_o$), and the plasma ring to ($\phi + s_2 B_v^{(2)}$).

The primary circuit is constituted by n_1^o outer coils and n_1^i inner coils in series ; the equation of its current I_1 can be written :

$$\begin{aligned} &(n_1^o + n_1^i)\frac{d\phi}{dt} + n_1^o\left[s_1\frac{dB_v^1}{dt} + \frac{d\phi_o}{dt}\right] + n_1^i\frac{d\phi_i}{dt} \\ &+ (n_1^o R^o + n_1^i R^i) I_1 = V_1 \end{aligned} \qquad (13)$$

An energy equation has been written for the total plasma current $\vec{I}_p$, which becomes, after use of the flux of the Poynting vector $\vec{E} \wedge \vec{B}$:

$$\begin{aligned} &\frac{d\phi}{dt} + s_2\frac{dB_v^{(2)}}{dt} - 4\pi R \times 10^{-9}\,\text{Log}\left(\frac{bp}{a}\right)\frac{dIp}{dt} \\ &- 4\pi R \times 10^{-9}\,\text{Log}\left(\frac{bp}{b_\ell}\right)\frac{dI_\ell}{dt} + K\frac{d\Delta}{dt} = V \end{aligned} \qquad (14)$$

where $K = 2\pi R \times 10^{-8} B_v^{(2)} - 2\pi I_p \times 10^{-9} \left[\text{Log} \frac{bp}{a} + \frac{R}{bp} + \frac{l_i}{2} \right]$

V is the loop voltage at the boundary of the plasma, I_ℓ the homogeneous vacuum vessel current, b_ℓ the minor radius of this vessel and bp an equivalent minor radius of the magnetic circuit assimilated to a torus.

The preprogramming circuit and the feedback circuit, required for plasma equilibrium, are made of inner and outer coils mounted in opposition and with the same number of inner and outer turns so as not to induce flux in the iron core. Let n_{PR} be the number of inner or outer coils for the preprogramming windings and n_f the one for the feedback system. The equations of their currents I_{PR} and I_f can be written :

$$n_{PR} \left[s_1 \frac{dB_v^{(1)}}{dt} + \frac{d\phi_o}{dt} - \frac{d\phi_i}{dt} \right] + L \frac{dI_{PR}}{dt} + \left[n_{PR}(R_o + R_i) + R \right] I_{PR} = V_{PR} \qquad (15)$$

$$n_f \left[s_1 \frac{dB_v^{(1)}}{dt} + \frac{d\phi_o}{dt} - \frac{d\phi_i}{dt} \right] + n_f (R_o + R_i) I_f = V_f \qquad (16)$$

where L and R are the self-inductance and the resistance necessary to uncouple the preprogramming and feedback systems.

At last the equation of the homogeneous current I_ℓ of the vacuum vessel can be written, by evaluation of the flux between itself and the plasma :

$$- 4\pi R \times 10^{-9} \text{Log} \frac{b_\ell}{a} \frac{dIp}{dt} + R_\ell I_\ell + K' \frac{d\Delta}{dt} = V \qquad (17)$$

As the Tokamak has a configuration of nested tori, linear combinations of the circuits equations have been solved in fact, where the fluxes between these tori have been made obvious. This has been made to avoid singularity in the matrix of the system.

It is of course necessary to associate to this system the equilibrium equation ; taking into account the fact that the time constant of the eddy currents in the liner is small relatively to the plasma current rise time, the equation (12) is taken as equation of Δ even when the currents are time dependent.

In the formule (9) of $B_v^{(3)}$, one must take :

$$I_o = n_1^o I_1 + n_{PR} I_{PR} + n_f I_f$$

$$I_i = n_1^i I_1 - n_{PR} I_{PR} - n_f I_f + I_{Bz}$$

where I_{Bz} is the constant premagnetizing current necessary to have a flux swing of 2V x S.

In the formula (10) of B_{eq}, as the plasma is assumed to be always tangent to the limiter, whose minor and major radii are a_D and R_o, we have :

$$a = a_D - |\Delta|$$

$$R = R_o + \Delta$$

If we set $I' = \{ I, \Delta \}$ and if we derive equation (12), then the whole system of equations (12) to (17) can be written :

$$M(t, I', \beta, l_i) \frac{dI'}{dt} + R(t, I', \beta, l_i) I' = f(t, I', V) \qquad (18)$$

where M and R are (6 x 6) matrix and f a 6 variables vector. The quantities β, l_i, V are derived from a plasma transport code which is coupled to the system (18). The system thus defined and solved by a predictor-corrector method enables to simulate the currents with a precision of about 10 %. Figure 14 gives as an example the comparison between experiment and calculation of the plasma current and loop voltage.

It is then possible to solve the equilibrium problem : we desire the plasma position Δ to be as close as possible to a certain reference Δ_{ref}. So we are led to minimize $B_v^{(3)}(\Delta_{ref}) - B_{eq}(\Delta_{ref})$. The first control parameter is the proportion of inner and outer turns of primary coils. Let α be the ratio of outer turns to the total number of turns of the primary windings. We search α_o such that :

$$J(\alpha_o) = \inf_{0<\alpha<1} J(\alpha) \quad \text{with} \quad J(\alpha) = \int_o^T |B_v^{(3)}(\Delta_{ref}) - B_{eq}(\Delta_{ref})|^2 \, dt$$

T being the duration of the discharge.

The ratio α_o being now fixed ($\alpha_o = 0{,}55$), the second stage is to find the preprogramming voltage $V_{PR}^o(t)$ that minimizes J again, this voltage being bounded at each instant by the maximum voltage V_{max}. The optimal control problem is then to find V_{PR}^o such that :

$$J(V_{PR}^o(t)) = \inf J(V_{PR}(t))$$

$$|V_{PR}| \leq V_{max}$$

The state of the system being given by (18).

This problem being solved, it is necessary to find if this equilibrium is stable or not. The stability condition is :

$$n_{Bv} < n_{Beq} \qquad (19)$$

where n_{Bv} and n_{Beq} are the index of the magnetic fields $B_v^{(3)}$ and B_{eq}

$$n_{Bv} = - \frac{R}{B_v^{(3)}} \frac{\partial B_v^{(3)}}{\partial \Delta} \quad , \quad n_{Beq} = - \frac{R}{Beq} \frac{\partial Beq}{\partial \Delta}$$

It has been proved[6] that n_{Bv} is approximately equal to :

$$n_{Bv} \simeq - \frac{10\,R^2}{\mathrm{Log}\frac{8R}{a} + \beta + \frac{li}{2} - 1{,}5} \left[\frac{b(\phi,\Delta,\beta,li)}{Ip} \frac{\partial Ip}{\partial \Delta} + \frac{db}{d\Delta}(\phi,\Delta,\beta,li) \right] \quad (20)$$

where $b(\phi,\Delta,\beta,li) = b_p^{(3)}(\phi,\Delta,\beta,li) + \alpha b_e^{(3)}(\phi,\Delta) + (1-\alpha) b_i^{(3)}(\phi,\Delta)$

The contribution of $\frac{\partial b_p^{(3)}}{\partial \Delta}$ in n_{Bv} is almost 3 ; the attraction of the plasma by the core has therefore a very important destabilizing effect. The contribution of $\frac{db_e^{(3)}}{d\Delta}$ and $\frac{db_i^{(3)}}{d\Delta}$ is very small ; therefore the inner coils and outer coils, which are very far from the plasma, have no influence on its stability.

The stability diagram is given on Fig. 13 and the necessity of a feedback system[6,7] to ensure a broader stability range and a larger stability margin is obvious.

We can see, in conclusion, the necessity of a precise description of the magnetic field generated by the various windings including the plasma itself with the real current density distribution and pressure, in presence of the transformer core, to solve the plasma equilibrium problem, and the importance of a good knowledge of the derivatives of these fields with respect to the plasma position to solve the stability problem.

5. ACKNOWLEDGEMENTS

The authors are grateful to C. Leloup for the discussions they had with him on this problem, to J. Le Foll and B. Thooris for their work on the code MAGNETIX, to M. Pariente for his contribution to the code POISSON, to P. Lecoustey and to P. Plinate for the measments they made on TFR, to C. Mercier, A. Samain and M. Dubois for the discussion on the equilibrium problem.

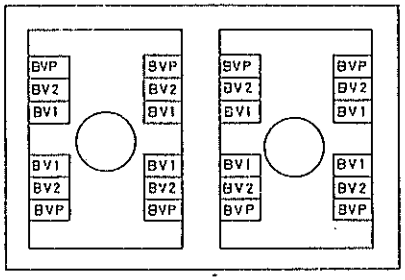

- Fig. 2 -

BVP : primary coils
BV1 : feedback coils
BV2 : preprogrammed field coils

REFERENCES

1. Equipe TFR - Le Tokamak TFR 600 - Report EUR - CEA - FC - 916 - (1977)

2. V.D. Shafranov - Plasma Equilibrium in a Magnetic field - Reviews of Plasma Physics - 2 - p 103-151 (1970)

3. K. Halbach - Proc 2nd Int. Conf. on Magnet. Technology - Rutherford Laboratory (1967)

4. R. Aymar - C. Leloup - M. Pariente - Equilibrium field and current determination for Tokamaks - Report EUR - CEA - FC - 821 - (1977)

5. J. Le Foll - B. Thooris - Code 2D MAGNETIX - Rapport CISI Saclay (à paraître)

6. J. Blum et al - Developments of the Makokot code I - Equilibrium of a plasma without a copper shell ant its stability - 2. Impurities in the noncoronal - equilibrium regime and hollow profiles. 7th controlled Nuclear Fusion Research - IAEA - CN 37 F6 (1978)

7. J. Blum - R. Dei Cas - J.P. Morera - P. Plinate - Influence of the iron core on plasma equilibrium and stability in TFR 600, a Tokamak without copper shell - Description of the fast feedback system - 10th Symposium an Fusion Technology - Padova (1978)

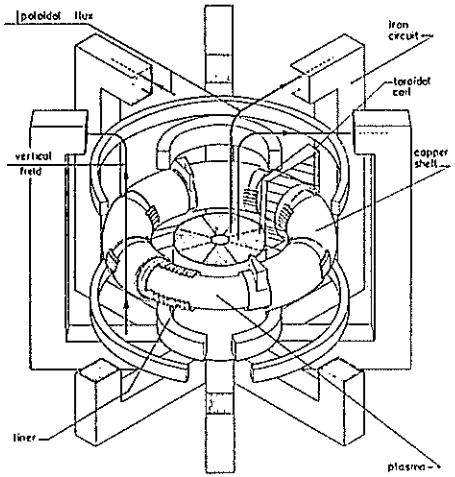

Fig. 1 - TOKAMAK CONFIGURATION

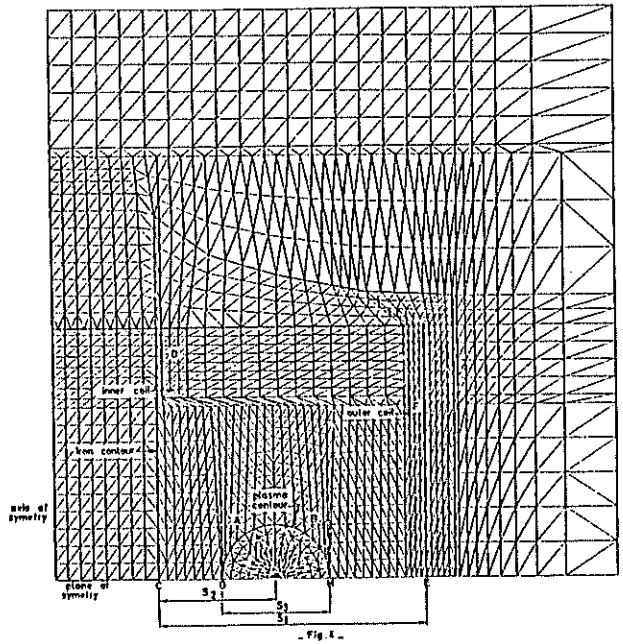

_ Fig. 4 _

MESH USED IN THE MAGNETIX CODE

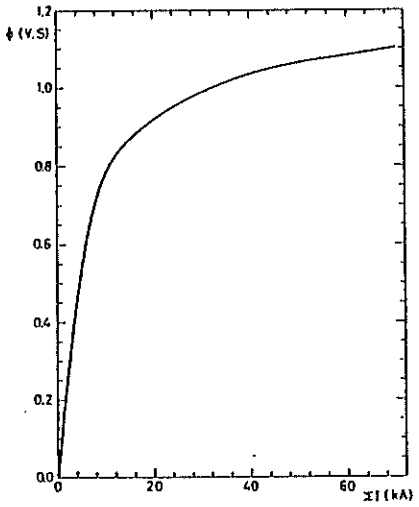

_ Fig. 6 _

FLUX IN THE IRON CORE VERSUS THE MAGNETIZING CURRENT.

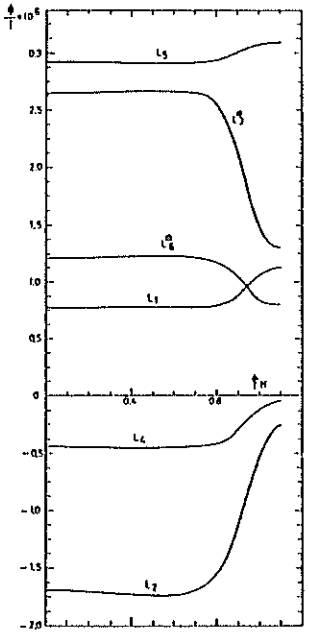

_ Fig. 7 _

LEAKAGE FLUX AT DIFFERENT POSITIONS

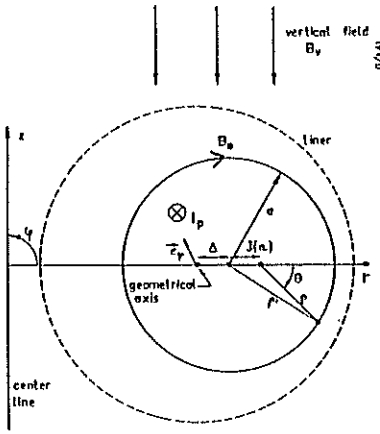

_ Fig. 3 _

CO_ORDINATE SYSTEM

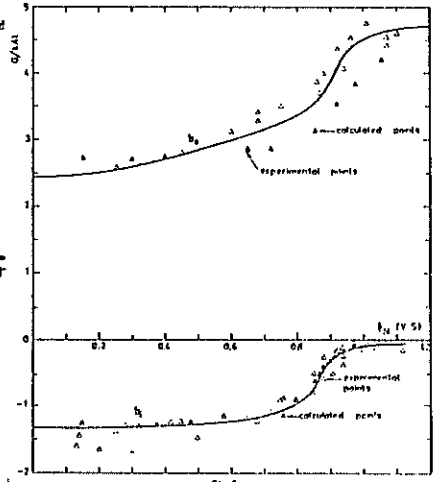

_ Fig. 5 _

COMPARISON BETWEEN MEASURED AND CALCULATED STRAY FIELD VALUES AS A FUNCTION OF THE IRON CORE FLUX

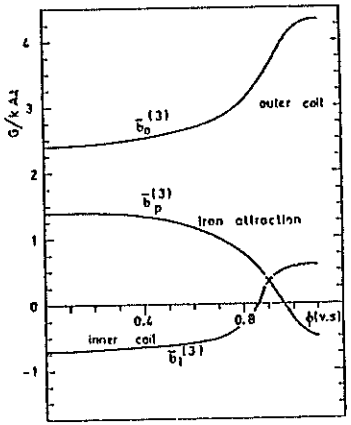

_ Fig. 8 _

VERTICAL FIELDS PRODUCED IN THE PLASMA REGION BY THE INNER AND OUTER COILS AND THE IRON CIRCUIT AS A FUNCTION OF THE FLUX

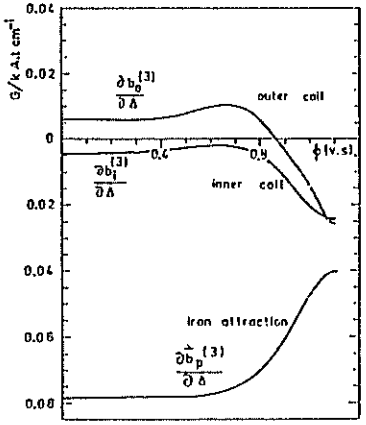

_ Fig. 9 _

GRADIENTS OF THE VERTICAL FIELD

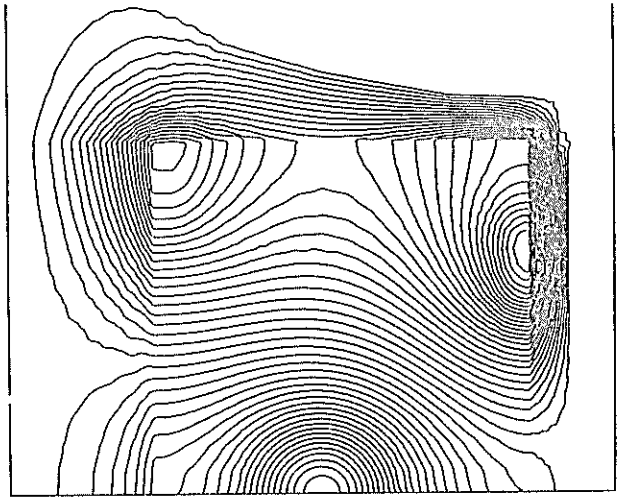

Fig. 10

EQUILIBRIUM CONFIGURATION FOR A 202 kA PLASMA CURRENT WITH PARABOLIC CURRENT DENSITY AND $\beta = 0.5$
NON SATURATED CASE $\phi_N = 0.13$ V.S, $I_0 = -97.57$ kA, $I_i = -108.47$ kA

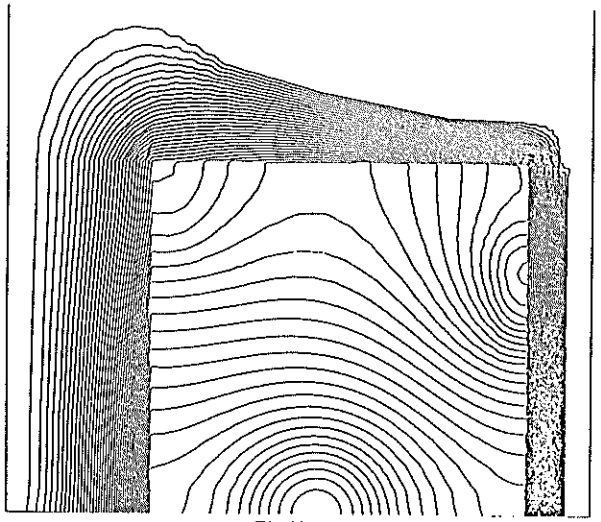

Fig. 11

EQUILIBRIUM CONFIGURATION IN A SATURATED CASE $\phi_N = 1.17$ V.S
$I_p = 202$ kA, $I_0 = -98.2$ kA, $I_i = -87.8$ kA.
PARABOLIC CURRENT DENSITY, $\beta = 0.5$

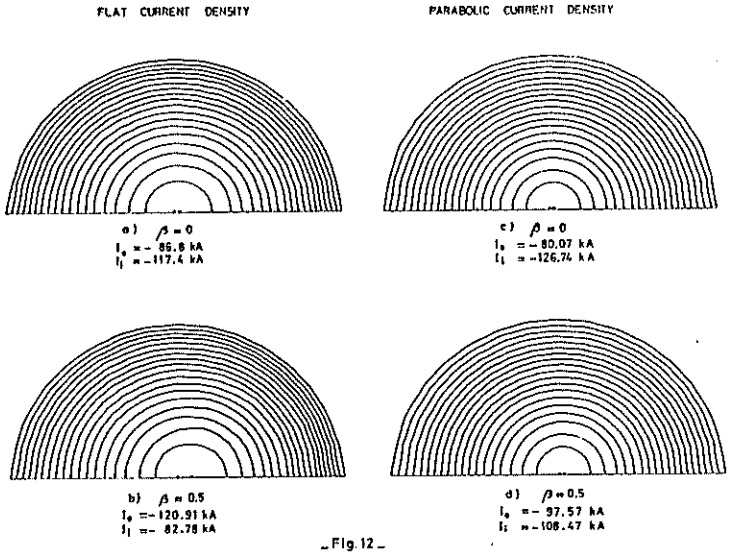

Fig. 12

MAGNETIC SURFACES INSIDE THE PLASMA IN NON SATURATED CASES. TOTAL PLASMA CURRENT 202 kA

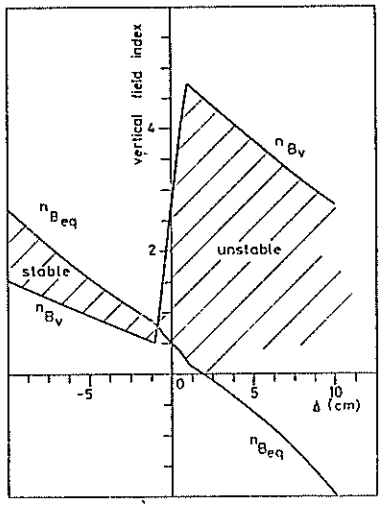

Fig. 13

STABILITY DIAGRAM WITHOUT FEEDBACK CONTROL

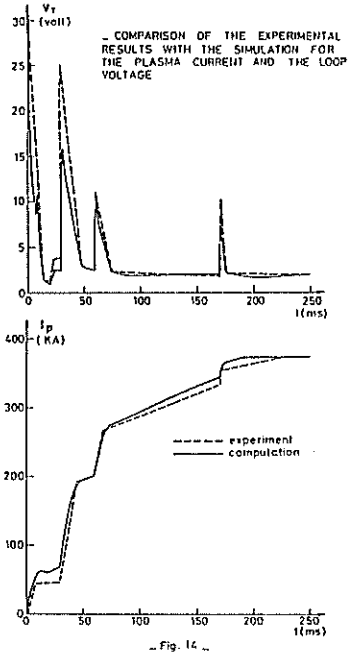

Fig. 14

COMPUTER DESIGN OF THE MAGNETIC FIELD OF A TRANSVERSE WIGGLER

A.U. Luccio
INFN - Laboratori Nazionali di Frascati, Italy

G.Pasotti and M. Ricci
CNEN - Laboratori Nazionali di Frascati, Italy

ABSTRACT

A transverse wiggler magnet for the storage ring Adone has been designed by means of two- and three-dimensional computer codes. Some of the difficulties involved with such magnetic structure, which would tend to perturb the stability of the electron beam, have been successfully overcome. The magnet has resulted in a rather unconventional design.

1. INTRODUCTION

A beam of relativistic electrons of kinetic energy E in a magnetic field B travels along a curved path with radius ϱ given by

$$\varrho[m] = 1.703\ 10^{-3}\ \gamma/B[T]\ , \qquad (1)$$

where $\gamma = E/m_o c^2 + 1 \simeq 1957\ E$ GeV .

A continuous spectrum of synchrotron radiation is emitted, with a critical photon energy[1]

$$\varepsilon_c[KeV] = 1.722\ 10^{-7}\ \gamma^2 B \qquad (2)$$

and total power, per mA of beam and mm of trajectory

$$\frac{d^2P}{dI\ ds}\left[\text{watt/mA/mm}\right] = 3.3115\ 10^{-10}\ \gamma^2 B^2\ . \qquad (3)$$

From Eqs.(2) and (3) above, it appears that to obtain high frequency photons and high power, both electron energy and magnetic field should be made as high as possible.

Synchrotron radiation is currently being produced by electron storage rings, characterized by high beam intensity and stability. High field regions are obtained in these machines, by inserting in their straight sections so called wiggler magnets, consisting of an array of alternating pole couples (transverse wigglers) or of a two-wire helical superconducting winding (helical wigglers).

For the 1.5 GeV electron storage ring Adone, a 1.8 tesla transverse wiggler has been studied, to be inserted in a 2.5 m long straight section. The design of the magnetic circuit has been thoroughly done by computer, at first with a two-dimensional code, and then with the three-dimensional GFUN[2]. Problems arisen in this design are here discussed.

2. MAGNET REQUIREMENTS

To make use of existing power supply and with regard to the geometrical constraints imposed by Adone, such as the length of the straights (2.5 m) and minimum vertical thickness of the donut in the wiggler area (4 cm), first design goals were:

6 poles (5 full + 2 half-poles); $B \geq 1.8$ tesla; $I \simeq 14 \times 4500$ A/pole.

A magnetic structure was thence designed preliminarly (Fig.1), to be improved to match the following requirements:

1 - highest value of $I_2 = \int B^2\ ds$;

2 - first field integral vanishing

$$I_1 = \int B\ ds = 0\ , \qquad (4)$$

along the longitudinal section of the magnet, independent of the field level;

3 - maxima of B as equal to each other as possible in each magnetic gap;

4 - field as homogeneous as possible along the radial (x) coordinate.

Requirement 1- above means an high radiation power output, according to Eq.(3). Once the wiggler structure has been optically matched into the Adone lattice[3], requirement 2- is to be met to ensure that the magnet will not perturb the stability of the electron beam. Fig.2 shows the effect of a non-vanishing field first integral on the trajectories of a "central" electron in the wiggler, i.e. of an electron injected on the axis of the wiggler, with speed parallel to it.

The electrons are injected into the storage ring Adone with an energy of 320 MeV. Thereafter the energy is brought gradually to the operational value, ranging between 800 and 1600 MeV. The magnetic field in the wiggler must increase at the same time to its maximum value, to avoid too large oscillations of the low energy beam in a strong field. It is clear that condition 2- above must be met at all field levels, which is an additional design difficulty.

Requirement 3- implies that the amplitudes of the beam radial oscillations be the same under each pole couple. This is a condition for the best matching of the phase-space brilliances of the synchrotron light emitted from the various wiggles[4].

3. MAGNET COMPUTER DESIGN

A first set of computer runs to analyze the structure of the wiggler magnet, as designed preliminarly by our engineers, has been performed by means of the two-dimensional Poisson code[5].

The shape of a pole and the computed B values are shown in Figs.3 and 4. These calculations are of a limited value however, because each wiggler pole piece is far from being infinitely extended in the "other" direction , as required by Poisson. These runs gave nonetheless us the confidence that the design of the poles was basically right, and were used to obtain a feeling on the effect of the corrections to be obtained by trimming pole gaps and adding correction current coils.

Pole basic shape and coil geometry thus frozen, our next step was that of optimizing the yoke design to fulfill the requirements 1- to 4- described above ,for the magnetic field.

This task was accomplished by means of the three-dimensional computer code GFUN, and involved several runs and a rather large computer and man time. From the beginning it appeared that designing a transverse wiggler of this proposed type met two main problems:

a - the structure was so magnetically compact that the coupling between poles made it difficult to change the field in a given position, by means of correcting coils or by varying the gap, without perturbing the field somewhere else. This in turn caused the making $I_1=0$ at all field levels very hard.

b - Each magnetic gap could be varied only in one way, i.e. by widening it. This made it difficult to match conditions 1- (high field) and 3- (equal field maxima) together.

It was clear that the degrees of freedom to play with were not enough, and that we had to give up with some of the basic requirements. Relying upon the feeling that the optics of the synchrotron radiation could be managed satisfactorily in every case, we decided to move towards optimizing the design mainly to fulfill Eq.(4) at all field levels and to get the value of the I_2 integral as large as possible.

Our first attempt was to decouple magnetically pairs of far-away poles. Fig.5 shows a sketch of field lines for the original geometry. In this, the return path for the magnetic field in each pole couple took place through the adjacent pole couples and gaps. It is apparent how a certain amount of flux couples e.g. pole (0) with the half-poles (3) and (4).

Some insight into the situation was obtained by means of a resistance network analogous (Fig. 6).

The following steps were then taken, starting from the original geometry depicted in Fig.1 (run id = WM, see also Table I):

α - return flux bars were attached to the sides of the magnet, thus making a series of H-shaped structures (run ids = WW and W1);

β - cuts were made on the main yoke, to minimize magnetic coupling between far poles (run ids = TOB2 through TOB15).

This latter scheme resulted in the "Toblerone" design, or "chocolate bar" shown in Fig.7. The TOB geometry we found capable of giving satisfactory answers to all 4 requirements of sec.2. On the contrary, corrections on the original WM and on the H-structures WW and W1 were not effective.

The results obtained with the structure of Fig.7 are shown in the Figs.8 to 12. Fig.8 shows the vertical field component on the longitudinal axis of the wiggler as a function of the coordinate, for various values of main coil current (uncorrected). As the figure shows clearly, the maxima of B under each pole are different (however the said geometry gives the best situations we could obtain).

Fig. 9 shows the field integrals $\int B\,ds$ for the various curves of Fig.8. With no current in the correction coils, these integrals have non-zero values. The figure shows as our design aims at giving with no corrections a low value for $\int B\,ds$ for the highest values of the main exciting currents.

Fig.10 gives the results of systematic calculations of the correction currents to obtain a vanishing field integral at all field levels. These calculations were performed by varying the current in the central pole main coil only. The maximum relative correction is $\sim$ -2500 A-turns, which appears obtainable with no difficulty. It is also clear, even if we did not pursue this in detail because of the high cost of GFUN calculations, that the same general corrections could be also obtained by

γ - inserting correction coils on each pole;

δ - changing the pole gaps somewhere (e.g. under the central pole), to equalize better the curve of Fig.10;

ε - with the use of iron field clamps at the two ends of the magnet, to gain an additional control on the field integral.

Fig.11 shows the behaviour of the field value under the central pole, as a function of the corrected current, according to Fig.10.

Fig.12 gives finally, for the corrected values of the current, the second field integral $\int B^2\,ds$. This is proportional to the synchrotron radiation power emitted by the wiggler, per unit electron beam current, from Eq.(3), through

$$\frac{dP}{dL}\left[\text{watt/mA}\right] = 3.312\ 10^{-7}\ \gamma^2 \int B^2 ds \ . \qquad (5)$$

From Fig.12, for example, it can be evaluated a synchrotron radiation output of $\sim$ 600 watt, at the maximum coil current of 7×4500 A-turns and an electron energy of 1.5 GeV ($\gamma \approx 3000$).

There is still a problem left: the homogeneity of the vertical component of the field B_y along a radius must be very stringent, if we like to have a first field integral vanishing at all radii (x). This in turn would enable us

a - to ensure that the field integral is also zero along the waving trajectory of the electrons in the wiggler; and

b - to move the beam across the wiggler at injection with its magnetic field already on.

Actually, as far as the condition a- is concerned, the field integral could be made zero along the trajectory also by giving it small non-zero and opposite values on two lines $x=x_1$ and $x=x_2$, bordering the radial oscillations of the beam. However, it is much more desirable to make B_y independent on the coordinate x, which will automatically cancel out the quadrupole term[4].

With the two-dimensional program Poisson, a study had been already made on the radial homogeneity of B_y [5]. Some of those results are shown in Fig.13, compared with three-dimensional GFUN results. With no correcting shims on poles the field is homogeneous radially, according to GFUN, within 10^{-3} only in a ± 5 cm wide region across the centerline of the magnet.

4. ACKNOWLEDGMENTS

We are indebted to our Colleagues of the Adone Group, and expecially to Prof. S. Tazzari, for so many discussions and helpful criticism during the development of this work.

5. REFERENCES

1. Jackson, J.D. Classical Electrodynamics. Wiley 1975, Ch. 14. Also Green, G.K. Spectra and Optics of Synchrotron Radiation. Brookhaven Nat. Lab. Report BNL 50522, April 15, 1976.

2. Newman, M.J., Simkin, J., Trowbridge, C.W., Turner, L.R. GFUN Users' Guide. Rutherford Lab. Report RHEL/R 244, September 1972. Also Proc. 5th Int. Conf. on Magnet Technology (MT-5). Roma, April 21-25, 1975.

3. Bassetti, M., Cattoni, A., Luccio, A., Preger, M. and Tazzari, S. A Transverse Wiggler Magnet for Adone. Proc. X Int. Conf. on High Energy Accelerators. Protvino, USSR, July 1977, Vol. II.

4. Luccio, A.U. Caratteristiche ottiche della luce di sincrotrone dal wiggler di Adone. INFN-Frascati, Div. Macchine. Memo E-24, 1978. Also Status Report on the Adone wiggler and X-ray beam line. Proc. Wiggler Meeting. Frascati June 29-30, 1978.

5. Luccio, A.U. Sul campo magnetico del wiggler di Adone. INFN-Frascati, Div. Macchine. Memo MA-30. Also Memo MA-30a, 1977.

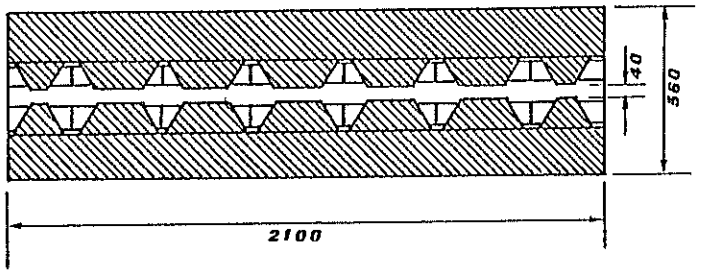

Fig.1. Six-pole wiggler. Preliminary magnetic structure.

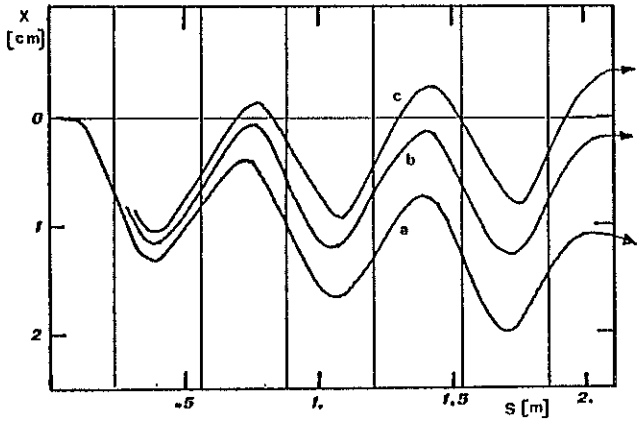

Fig.2. Computed electron trajectories through a six-pole wiggler for three field configurations with different first field integral $\int B\,ds$ values: a) = +523, b) = +39, c) = -203 G-m.

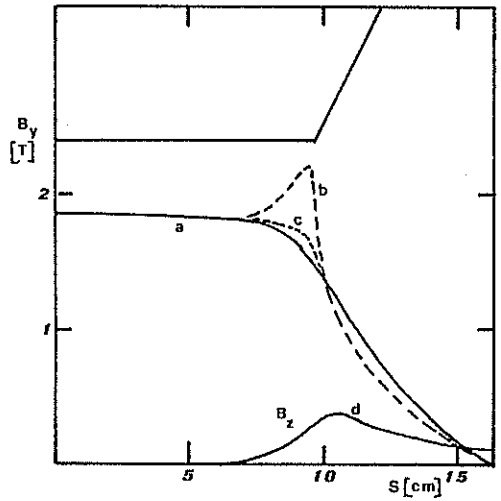

Fig.3. Vertical (y) and longitudinal (z) field shape on the longitudinal symmetry plane of the wiggler. Full pole. Two-dimensional Poisson runs. a) y = 0, b) y = 2 cm, c) y = 1 cm, d) y = 1 cm.

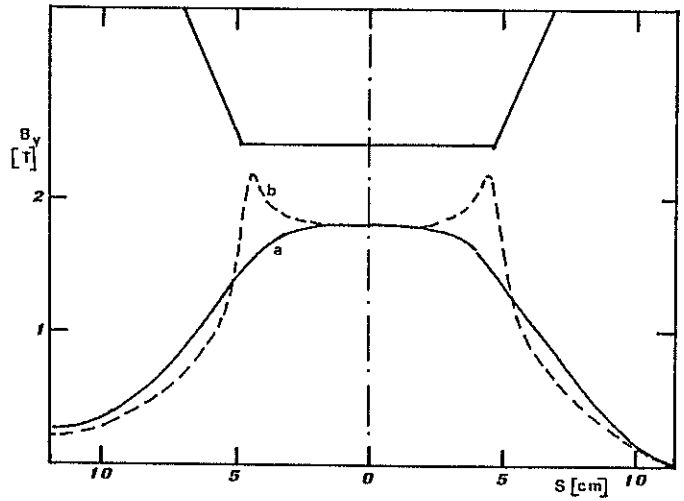

Fig.4. Vertical (y) field on the longitudinal symmetry plane of the wiggler. Half pole. Two-dimensional Poisson runs. a) y=0, b) y=2 cm.

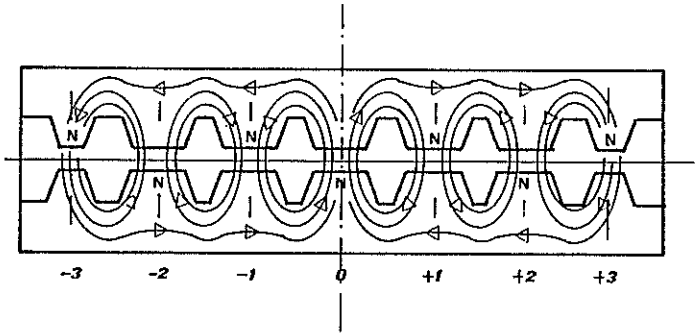

Fig.5. Wiggler schematic. Field lines pattern showing coupling between far-away pole couples.

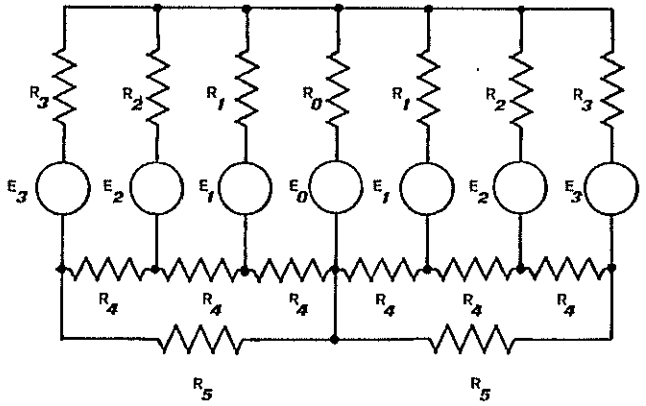

Fig.6. Linear electric network analogous for the reluctance magnetic network. Field pattern of Fig.5.

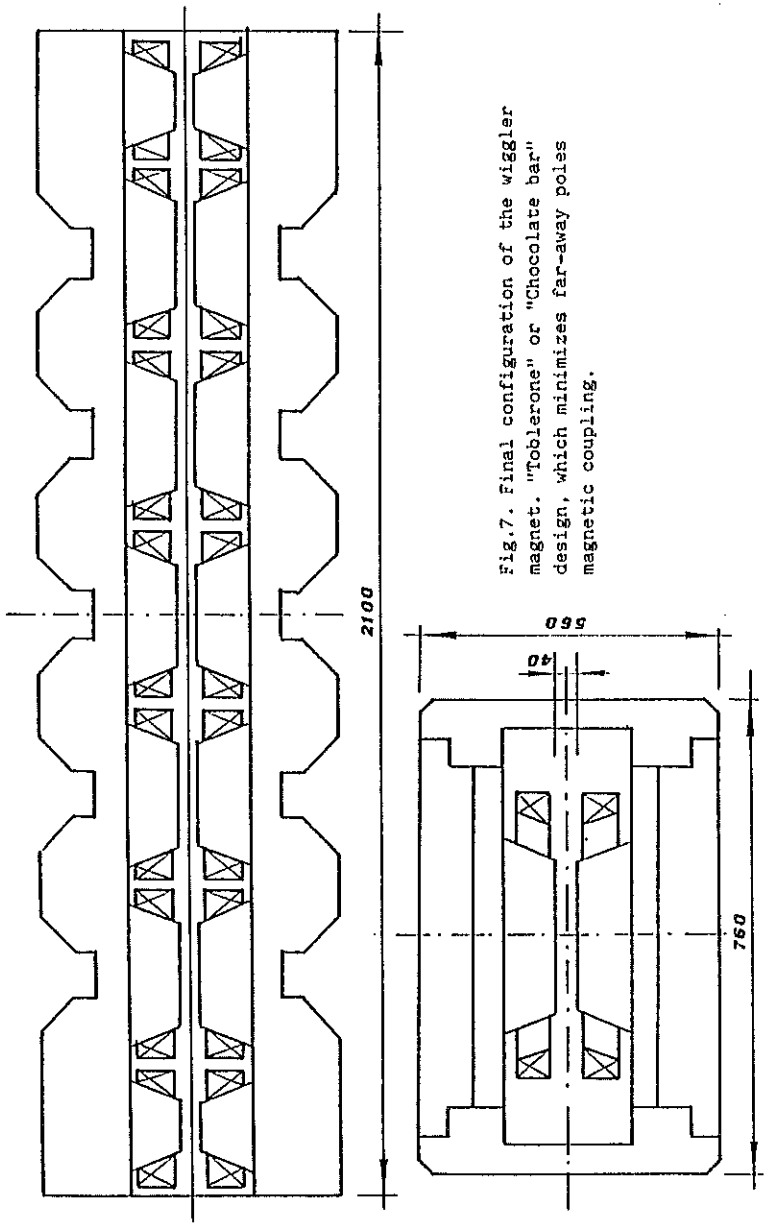

Fig.7. Final configuration of the wiggler magnet. "Toblerone" or "Chocolate bar" design, which minimizes far-away poles magnetic coupling.

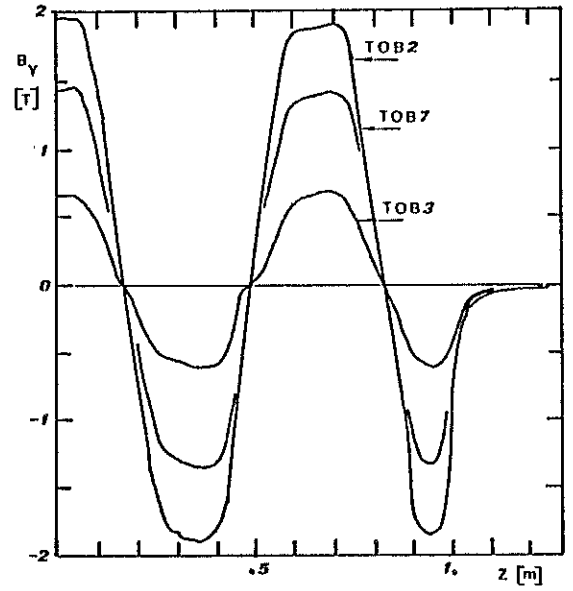

Fig.8. Vertical magnetic field in the wiggler along the x=y=0 axis. TOB2) I_o = 4500 A x 7 turns; TOB7) I = 0.7 I_o; TOB3) I = 0.3 I_o.

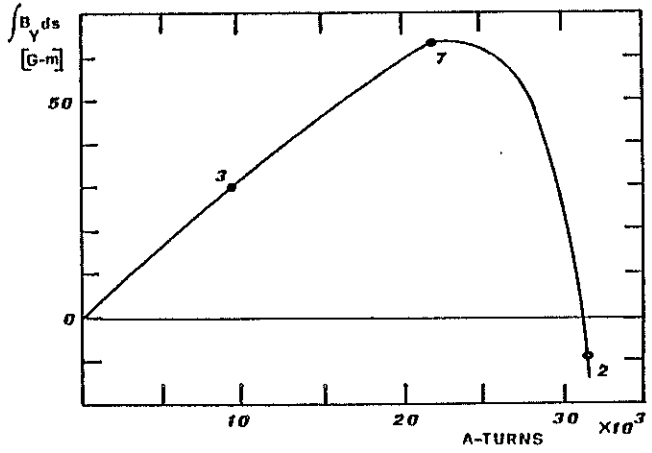

Fig.9. Field integral as a function of the excitation in the main coils (no correction currents).

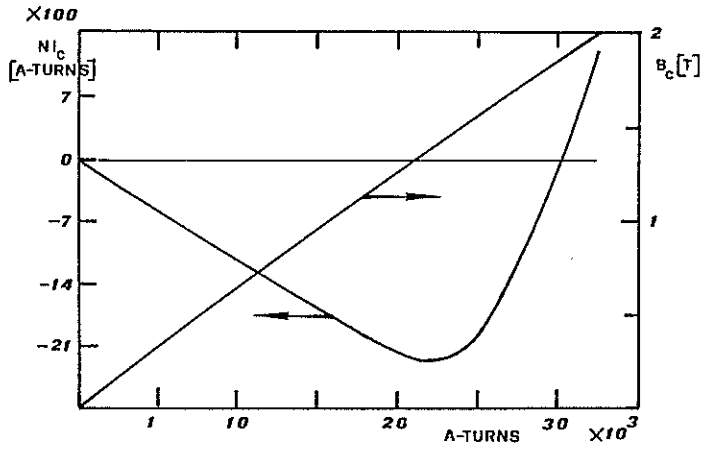

Figs.10 and 11. Correction ampere-turns as a function of main excitation, to achieve $I_1 = 0$ at all field levels (scale on the left). Field under center pole with corrected excitation.(scale on the right).

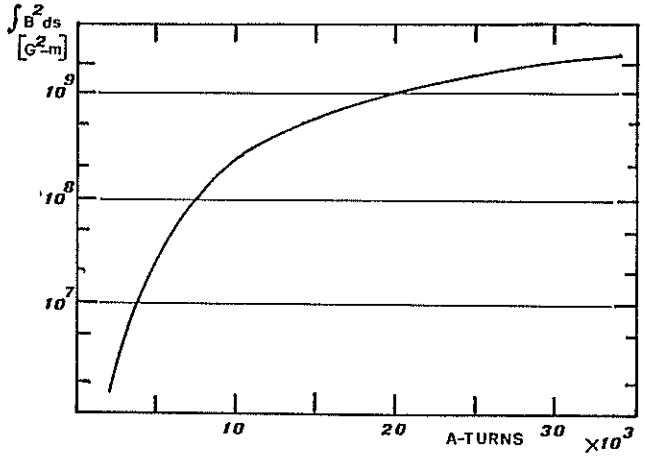

Fig.12. Second field integral in the wiggler as a function of main excitation, in the corrected conditions of Figs.10 and 11.

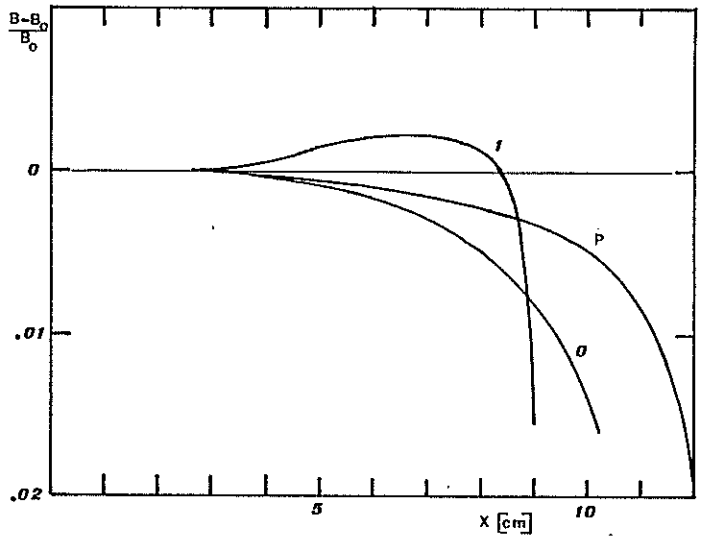

Fig.13. Radial inhomogeneity of the vertical field in the wiggler. No correcting shims on poles. 3-dimensional GFUN results are here shown for center (o) pole and next-to-center (1) pole. Poisson results are also shown for comparison.

SIMPLE MAGNETIC CALCULATIONS WITH COMMERCIAL FINITE ELEMENT CODES

Rob J.B. Reefman, Herman H.J. Lok, Theo G.M. Harink
Holec Switchgear Division, P.O. Box 23, 7550 AA Hengelo (O)
the Netherlands

ABSTRACT

The presented paper indicates how magnetic field analyses can be done by using standard software available at several software service companies and institutes. As an example some results are shown of the magnetic field analysis between two copper conductors placed in a harmonic axial magnetic field. Finite Element techniqeus deliver the solution of the magnetic vector potential whereas the magnetic induction is calculated following the usual way of flux- or stress data recovery in finite element codes.

1. INTRODUCTION

Magnetic induction has a great influence on the behaviour of the gas discharge between the contacts of a circuit breaker. In order to study this behaviour it is essential to know the magnetic induction between the contacts.
Placing an electrically conducting body in a harmonic magnetic field will cause eddy currents to be introduced in it. These currents generate a magnetic field which interferes with the original one. The solution of the resulting magnetic induction is achieved by using a description of the physical phenomenon in terms of the magnetic vector potential. The calculations have been made with two finite element programs: PAFEC 70$^+$ and MSC/NASTRAN. A new functional was added to PAFEC to face the Laplacian operator on the magnetic vector potential in cylindrical coordinates whereas in MSC/NASTRAN the analogon with thermal conduction was used and the Laplacian operator was performed in carthesian coordinates. The finite element discretisation in PAFEC was performed with linear triangular ring elements whereas in MSC/NASTRAN the discretisation was done with three dimensional solid elements, eight node bricks. In order to save costs in these three dimensional calculations in MSC/NASTRAN the standard provisions are used to take advantage of axial geometric symmetry. This provision is called cyclic symmetry. The calculation of the magnetic induction, containing linear combinations of the derivatives of the magnetic vector potential, follows the normal routine of flux- or stress data recovery. Via a small Fortran program the various derivatives are collected afterwards, correctly added, transformed back to the time domain and put into formats which can be used by standard (for example NASTRAN) plot routines.

2. MATHEMATICAL FORMULATION

2.1. THE MAGNETIC VECTOR POTENTIAL EQUATION

Neglecting the dielectric displacement current and assuming a linear relationship between the magnetic induction $\vec{B}$ and the magnetic field strength $\vec{H}$ the magnetic induction is determined by the following equations (Maxwell):

$$\nabla * \vec{E} = -\frac{\partial \vec{B}}{\partial t}$$
$$\nabla * \vec{B} = \mu \vec{J} \qquad 1)$$
$$\vec{J} = \sigma \vec{E}$$

The first equation of 1) with the definition of the magnetic vector potential $\vec{A}$:

$$\vec{B} = \nabla * \vec{A} \qquad 2)$$

leads to an equation for the current density of

$$\vec{J} = \sigma \vec{E} = -\sigma \frac{\partial \vec{A}}{\partial t} + \sigma \nabla \varphi$$

The current density part $\sigma \nabla \varphi$ is not influenced by the magnetic field so it is the part without eddy currents and it is expressed as the electrical current density $\vec{J}_e$ so

$$\vec{J} = -\sigma \frac{\partial \vec{A}}{\partial t} + \vec{J}_e \qquad 3)$$

Substituting the magnetic vector potential definition 2) in the second equation of 1) will lead, together with 3) to

$$-\nabla\nabla.\vec{A} + \nabla^2\vec{A} - \sigma\mu \frac{\partial \vec{A}}{\partial t} + \mu \vec{J}_e = 0$$

The divergence of A equals :

$$\frac{\partial A_x}{\partial x} + \frac{\partial A_y}{\partial y} + \frac{\partial A_z}{\partial z} = \frac{1}{r}\frac{\partial}{\partial r}(rA_r) + \frac{1}{r}\frac{\partial A_\theta}{\partial \theta} + \frac{\partial A_z}{\partial z}$$

and since the considered problem is an axial-symmetrical one, in which only the term Aθ exists independently of angle θ, the divergence of $\vec{A}$ is equal to zero so the above equation becomes

$$\nabla^2\vec{A} - \sigma\mu \frac{\partial \vec{A}}{\partial t} + \mu \vec{J}_e = 0 \qquad 4)$$

Because of dealing with harmonic changing fields it is sensible to transform the formulae from the time domain into the complex domain:

$$\vec{J} = -j\omega\sigma\vec{A} + \vec{J}_e \qquad 5)$$
$$\nabla^2\vec{A} - j\omega\sigma\mu\vec{A} + \mu\vec{J}_e = 0 \qquad 6)$$

The word "simple" in the title of the paper points to a constant permeability (μ) for each element. If the permeability was not a constant for each element, this would lead to a much more complicated set of equations as the three uncoupled diffusion equations given by 6).

2.2. THE SOLUTION IN THE FORM OF A STATIONARY QUADRATIC FUNCTIONAL

For a Hilbert space it can be proved [1,2] that if the operator L, applied in the equation Lv = f, is linear and positive, the quadratic functional F:

$$F = (Lv,v) - (f,v) - (v,f) \qquad 7)$$

is stationary ; and vice versa if F is stationary than follows Lv = f.
Following the finite element text books it is quite obvious to take as operator L on v:

$$Lv = -\nabla^2 v + j\omega\sigma\mu v \qquad 8)$$

and define the scalar product (u,v) as

$$(u,v) = \iiint_V u v^* dV \qquad 9)$$

This means that if the above requirements are fulfilled the requirement of F to be stationary is the same as $\nabla^2 v - j\omega\sigma\mu v + f = 0$
An investment of the scalar product (Lv, v) results in

$$(Lv,v) = \iiint_V |\nabla v|^2 + j\omega\sigma\mu |v|^2 dV - \iint_S (\nabla v)\vec{n} v^* dS$$

If the domain is large the value of v, representing a potential, will vanish on the boundary so the surface integral will vanish. However, the results mean that the operator L is not positive so the statement of the functional has no sense. This problem can be avoided by defining another operator L' as

$$L' = \begin{pmatrix} D & -\omega\sigma\mu \\ \omega\sigma\mu & D \end{pmatrix} \qquad 10)$$

in which Dv is defined as $Dv = -\nabla^2 v$

This operator is applied to a vector $\{v\}$ equal to $\begin{Bmatrix} v1 \\ v2 \end{Bmatrix}$ in which v1 stands for the real part of v and v_2 stands for the imaginary part.

It can easily be shown that together with the vector $\{f\}$ equal to $\begin{Bmatrix} f \\ 0 \end{Bmatrix}$ this will lead to a quadratic functional in the meaning as mentioned before.

So $$L'\{u\} = \{f\} \qquad 11)$$

What is actually done by this excercise is splitting the complex equation into two real equations, one for the real part and one for the imaginary part. This is the way the solution is performed, however, for readers convenience the complex notation of the equations is maintained throughout the paper.

Two functionals will be considered one for carthesian coordinates and one for cylindrical coordinates.

The functional in carthesian coordinates is considered first. Since, dealing with the magnetic vector potential the Laplacian operator is applied to a vector. This means:

$$\nabla^2\vec{v} = \left(\frac{\partial^2}{\partial x^2} + \frac{\partial^2}{\partial y^2} + \frac{\partial^2}{\partial z^2}\right)\left(v_x\vec{i} + v_y\vec{j} + v_z\vec{k}\right) \qquad 12)$$

For each vector component, this operation gives the same result as for a scalar operation. Substitution of v = Ax and f = + μ Jex in 7) in the complex notation by using the rules of partial differentiating and applying Green's divergence theorem, will after some algebraic work lead to:

$$F_x = \iiint_V \left[\left(\frac{\partial A_x}{\partial x}\right)^2 + \left(\frac{\partial A_x}{\partial y}\right)^2 + \left(\frac{\partial A_x}{\partial z}\right)^2 + j\omega\sigma\mu A_x^2 - 2\mu\right]_{ex} R_e A_x \,dV - \iint_S (\nabla A_x)\vec{n} A_x^* \,dS$$

As for the considered problem the boundary condition is a zero value for all potentials, the surface integral vanishes so

$$F_x = \iiint_V \left[\left(\frac{\partial A_x}{\partial x}\right)^2 + \left(\frac{\partial A_x}{\partial y}\right)^2 + \left(\frac{\partial A_x}{\partial z}\right)^2 + j\omega\sigma\mu A_x^2 - 2\mu\right]_{ex} R_e A_x \,dV \qquad 13)$$

The same functional exists for a diffusion problem or a transient heat conduction problem. The functionals for the other components are identical.

For the cylindrical coordinate system only the e-component is considered. The Laplacian operator on this vector component works out as follows:

$\vec{V}_\theta = \vec{S}\, V_\theta(r,z,t)$

$\vec{S} = -\vec{i}\sin\theta + \vec{j}\cos\theta$

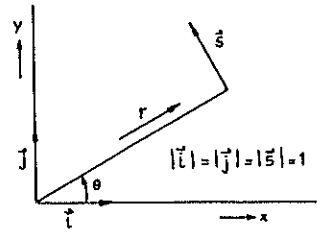

Fig. 1.

$$\nabla^2\vec{V}_\theta = \left(\frac{1}{r}\frac{\partial}{\partial r}r\frac{\partial}{\partial r} + \frac{1}{r^2}\frac{\partial^2}{\partial\theta^2} + \frac{\partial^2}{\partial z^2}\right)\left(-V_\theta\sin\theta\,\vec{i} + V_\theta\cos\theta\,\vec{j}\right)$$

and this operation gives

$$\nabla^2\vec{V}_\theta = \left(\frac{1}{r}\frac{\partial V_\theta}{\partial r} + \frac{\partial^2 V_\theta}{\partial r^2} - \frac{V_\theta}{r^2} + \frac{\partial^2 V_\theta}{\partial z^2}\right)\vec{s} \qquad 14)$$

This result is not the same as for a scalar. The difference is the term $-\frac{V_\theta}{r^2}$ which is not present with a scalar Laplacian operation.

And now the substitution of v = Ae and f = + μ Jee in 7) leads, after the same kind of algebraic work as was done for the carthesian coordinates, to:

$$F_\theta = \iint_S r\left[\left(\frac{\partial A_\theta}{\partial r}\right)^2 + \left(\frac{\partial A_\theta}{\partial z}\right)^2 + \frac{2A_\theta}{r}\frac{\partial A_\theta}{\partial r} + \frac{A_\theta^2}{r^2} + j\omega\sigma\mu A_\theta^2 - 2\mu\right]_{e\theta} R_e A_\theta \,dS$$

Because of the term $\frac{A_\theta}{r^2}$ this is not the same functional as is used for heat conduction problems. Thus standard finite element codes for heat conduction in cylindrical coordinates are not suitable to solve the equation of the vector potential unless the used functional is changed. And this is done by Harink in the program PAFEC 70+ [3].

The requirements of the functionals being stationary will be pointed out in the section of the finite element formulation.

2.3. A FINITE ELEMENT FORMULATION

2.3.1. THE SET OF EQUATIONS

The area in which the solution for the magnetic vector potential is to be calculated, is divided into a number of small areas of simple geometric forms like triangles or bricks. On the corners of the elements, and sometimes on other places too, nodes are specified. Connected elements have the same nodes on their common border [4]. With an interpolation function over the element, mostly polynomials, the variable on an arbitrary place in the element is expressed in the values of the nodes of the element. And these values are the unknowns to solve.

In matrix notation this can be expressed as:

$$\begin{aligned} v &= [N]\{v^e\} \\ \frac{\partial v}{\partial x} &= v_x = [N_x]\{v^e\} \\ \frac{\partial v}{\partial y} &= v_y = [N_y]\{v^e\} \\ \frac{\partial v}{\partial z} &= v_z = [N_z]\{v^e\} \end{aligned} \qquad 16)$$

Using the symbol for the magnetic vector potential and substituting these matrix expressions into the discussed functional gives for the case of the carthesian coordinates

$$F_x = \iiint_V \left[\{A_x^e\}^T[N_x]^T[N_x]\{A_x^e\} + \{A_x^e\}^T[N_y]^T[N_y]\{A_x^e\} + \{A_x^e\}^T[N_z]^T[N_z]\{A_x^e\} + \{A_x^e\}^T[N]^T j\omega\sigma\mu[N]\{A_x^e\} - 2\mu\right]_{ex}[N]\{A_x^e\}\,dV \qquad 17)$$

The requirement of Fx to be stationary means that the derivative of Fx to any of the unknowns, that means to any of the terms of vector $\{A^e\}$, has to be zero and that results in as many equations as there are terms of $\{A^e\}$.

In matrix form this can be written as

$$\frac{\partial F_e}{\partial \{A_x^e\}} = \iiint_V \left[[N_x]^T[N_x]\{A_x^e\} + [N_y]^T[N_y]\{A_x^e\} + [N_z]^T[N_z]\{A_x^e\} + [N]^T j\omega\sigma\mu[N]\{A_x^e\} - \mu]_{ex}[N]^T \right] dV = 0 \qquad 18)$$

The equations of all the elements are assembled in one functional that should be stationary. The set of equations can be written in a simpler notation by incorporating the integration:

$$[K]\{A_x^e\} - j\omega[M]\{A_x^e\} = \{P\} \qquad 19)$$

$[K]$ is known as the conduction matrix or stiffness matrix, $[M]$ is known as the heat capacity matrix or mass matrix and the vector $\{P\}$ is known as the load vector. In the case of this calculation of the magnetic vector potential the role of the mass matrix corresponds to the stiffness matrix. Therefore NASTRAN's possibility of changing the sequence of program modules, or insert or delete other NASTRAN modules, is used to multiply the massmatrix, once it has been assembled, by $j\omega$ and subtract it from the stiffness matrix $[K]$ [5]. Then the heat conduction sequence of modules was proceeded with a corrected stiffness matrix: $[K_c] = [K] - j\omega[M]$.

Once the set of equations is solved the gradients can easily be found by using 16). For simple linear elements as were used those gradients are constants for each element [4]. The calculated values are complex numbers. These complex numbers are the input of a very simple Fortran program which transforms the complex numbers back to the time domain, takes the right combinations of gradients to form the curl of the magnetic vector potential in order to find the vector components of the magnetic induction, and finally makes an NASTRAN acceptable input deck to plot the magnetic induction arrows by standard NASTRAN plot routines.

For the case of cylindrical coordinates a similar explanation could be written, except that it is not possible to use the standard heat conduction routines. Much work has been done, not only a new functional has been incorporated into PAFEC but also a complex solution procedure has been added and new plot routines have been written.

2.3.2. CYCLIC SYMMETRY

Consider a segment that is repeated n-times around an axis, like the shaded area in fig. 2 that is eight times repeated around the axis AX. If each segment had no common nodes with the other segments the total stiffness matrix would, in the case of the example, exist of eight identical blocks of coefficients grouped around the matrix diagonal. Because there is no coupling between the segments the system can be solved by handling one block of coefficients with different load vectors as is shown in fig. 3.

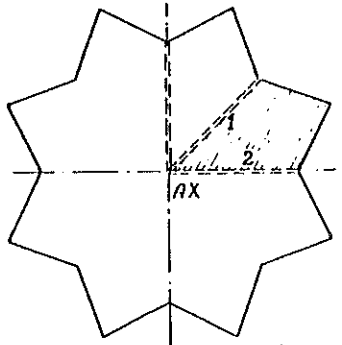

fig. 2 cyclic symmetry

And this procedure would save much computing effort. However, the connection conditions destroy this nice blocked situation of the matrix and the computing task is larger with all its consequences.

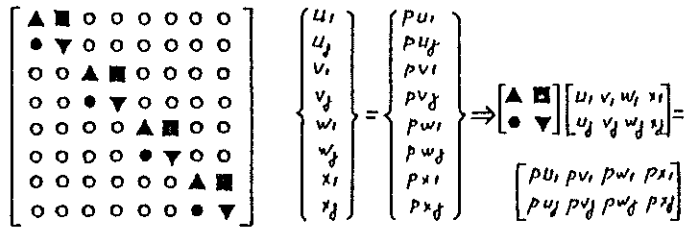

fig. 3 Symbolic representation of the set of equations for n identical not coupled segments.

Now by using symmetric components it is possible to solve the whole problem with the stiffness or coefficient matrix of one single segment. The method of symmetric components, published already long ago by Fortescue [7], is well-known by electrical engineers. The method is commonly used by fault calculations in three-phase electrical circuits.

The basis of the method is the statement that every asymmetric n-phase system can be constructed by n symmetric n-phase systems.

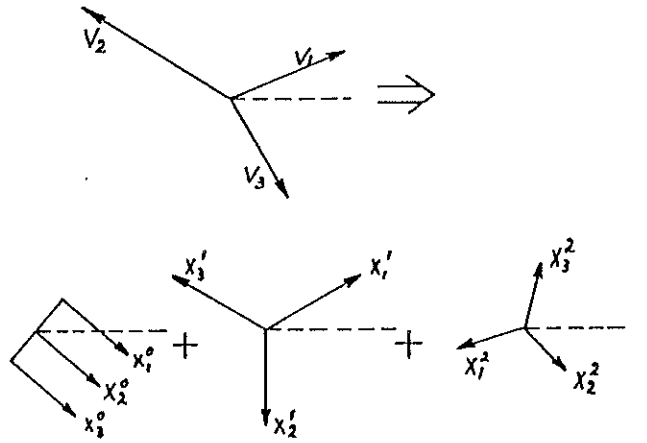

fig. 4 symmetric components

For instance, the asymmetric three phase system v_1, v_2, v_3, displayed in fig. 4, can be constructed by adding the three-threephase symmetric systems X^0 X^1 and X^2 shown in the same figure.

In formula $v_1 = X_1^0 + X_1^1 + X_1^2$

$v_2 = X_2^0 + X_2^1 + X_2^3$

$v_3 = X_3^0 + X_3^1 + X_3^2$

and because the systems are symmetric these equations can be written as

$$v_1 = X_1^0 + X_1^1 + X_1^2$$

$$v_2 = X_1^0 + X_1^1 e^{-j\frac{2\pi}{3}} + X_1^2 e^{-j\frac{4\pi}{3}}$$

$$v_3 = X_1^0 + X_1^1 e^{-j\frac{4\pi}{3}} + X_1^2 e^{-j\frac{2\pi}{3}}$$

And from this

$$X_1^0 = \frac{1}{3} v_1 + \frac{1}{3} v_2 + \frac{1}{3} v_3$$

$$X_1^1 = \frac{1}{3} v_1 + \frac{1}{3} v_2 e^{+j\frac{2\pi}{3}} + \frac{1}{3} v_3 e^{+j\frac{4\pi}{3}}$$

$$X_1^2 = \frac{1}{3} v_1 + \frac{1}{3} v_2 e^{+j\frac{4\pi}{3}} + \frac{1}{3} v_3 e^{+j\frac{2\pi}{3}}$$

can be obtained.

For an n-phase system can be written:

$$\{X\} = [T_{vx}] \{v\} \qquad 20)$$

$$\{v\} = [T_{xv}] \{X\} \qquad 21)$$

Instead of the voltage vectors of an electrical system, $v_1, v_2, \ldots v_n$ can be interpreted as the temperature, displacement or potential of a specific point in the n^{th} segment. The result of substituting 21) in the functional and assure its stationarity will be a set of equations with the symmetric components as unknowns.

$$[T_{xv}]^T [K_c] [T_{xv}] \{X\} = \{P\} \qquad 22)$$

Until here, there is no significant change in the situation. Only there exists another set of unknowns. But now transforming the segment connection conditions into symmetric components will show that it is possible to express these conditions in relationship between the symmetric components of the two sides of the segment that are connected with other segments (as indicated by 1 and 2 in fig. 2). The result of this excercise is: $(X^k)_{side\ 2} = (X^k)_{side\ 1} e^{jk\frac{2\pi}{n}}$ 23)

And this means that for solving this problem in symmetric components only the stiffness matrix of one single segment is necessary since by using relation 23) no coupling with the other segments are left. More computing effort can be saved for simple load conditions, for instance for a cylinder under hydrostatic pressure it will be only the X^0 component that supplies a contribution to the displacements so the other X components are zero and there is no need to calculate them. Symmetric components are a mighty feature in electrical engineering but it is a mighty feature in finite element use too; further details are given in the program manuals [6] .

3. PRACTICAL RESULTS

Experimental calculations were made with a coil of two solid copper conductor rings. The situation is displayed in fig. 5. The magnetic induction on the z-axis as a function of a dc current can easily be calculated by hand. The finite element discretisation (fig. 6) is performed with eight node solid bricks. In the circumferential direction 24 segments were chosen and by using the feature of cyclic symmetry only one of these segments was needed to discretisize. Only the positive z-axis was considered for symmetry reasons too. The potential values on the outer boundary in the radial and z directions were set on zero just as was done on the z-axis. The choice of the outer boundary is a matter of experience. The computer results of the dc calculation were really satisfactory in comparison with the analytical solution (fig. 7). The next calculation was a 50 Hz ac current calculation. Eddy currents in the solid copper rings cause a decrease of the magnetic induction and a phase delay with the precribed current. Measurement and computer calculation are shown in fig. 7. In comparison with other experimental calculations the expected inaccuracy of the magnetic induction in this case is 5 to 8%. Fig. 8 shows a plot of the magnetic induction vectors on a specific moment.

The following step was to bring two copper discs in the coil simulating the contacts of a circuit breaker. (Fig. 9).

The magnetic induction vector is plotted on several moments during the current loop. These plots are displayed in figures 10 to 17. Only the place of the copper disc is shown for that is the region of intrest.

There were no significant differences between the results of PAFEC with linear triangular elements and the NASTRAN results with the 3d solid elements. It may be concluded that commercial programs, even if these are not directly designed for the field of intrest, can offer an alternative for others who have no programming capacity and perhaps even to them who are accustomed to make their own programs. Considering the world of structural engineering it can be seen that the role of home made programs is mainly taken over by large general purpose packages and this may happen in electrical engineering too.

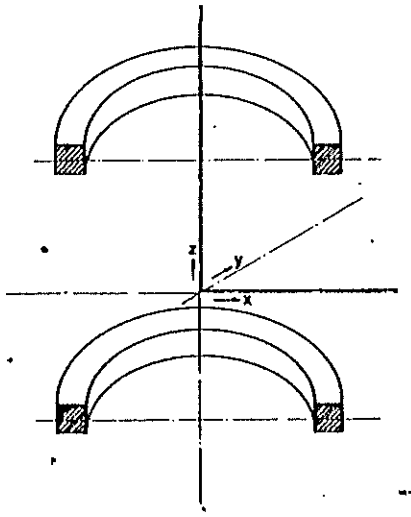

Fig. 5 The coil.

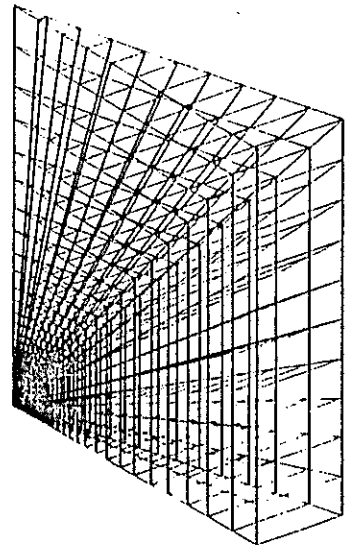

Fig. 6 the element discretisation of the coil

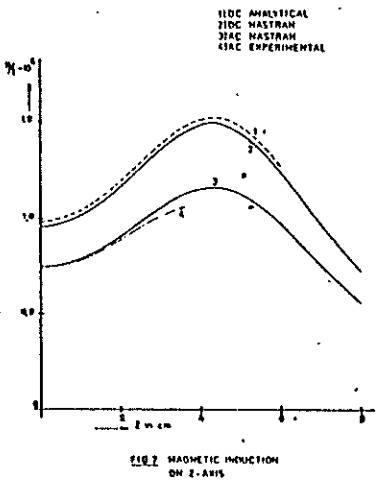

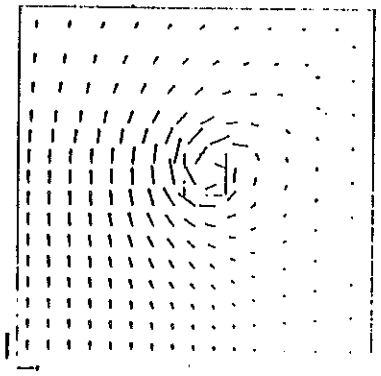

Fig. 8 the magnetic induction vector

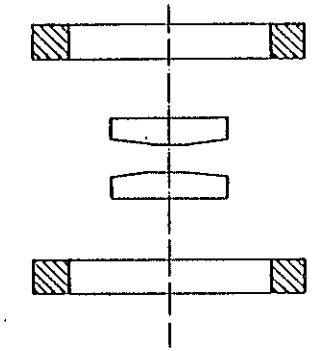

Fig. 9 The copper discs in the coil.

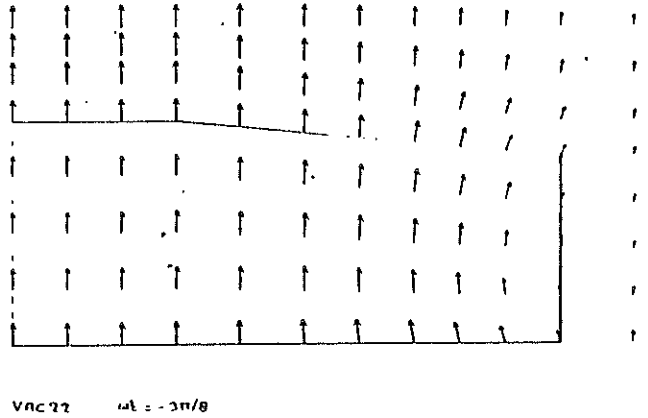

Fig. 10

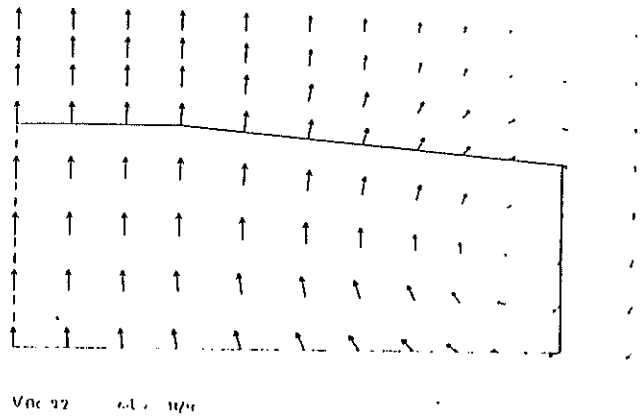

Fig. 11

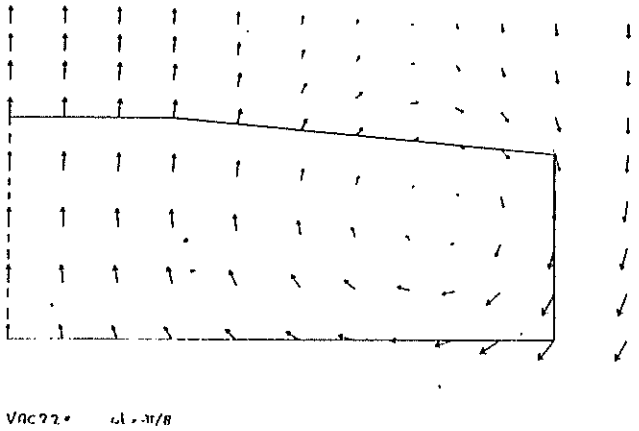

Fig. 12

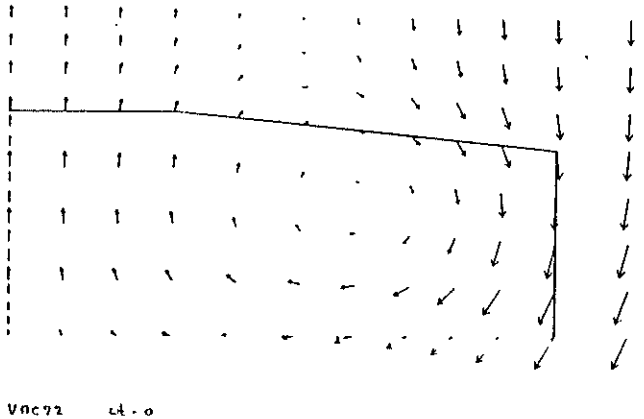

Fig. 13

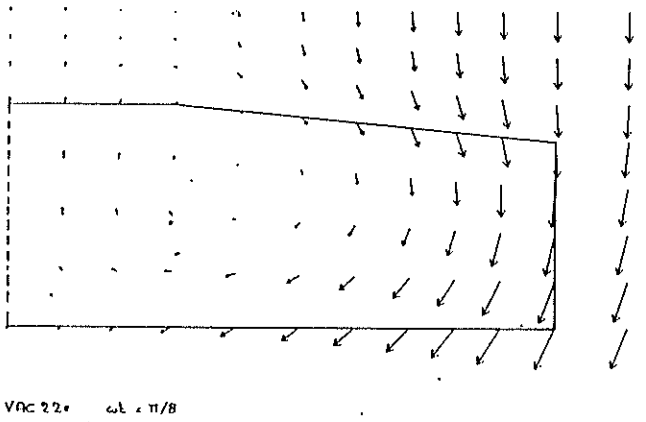

Fig. 14

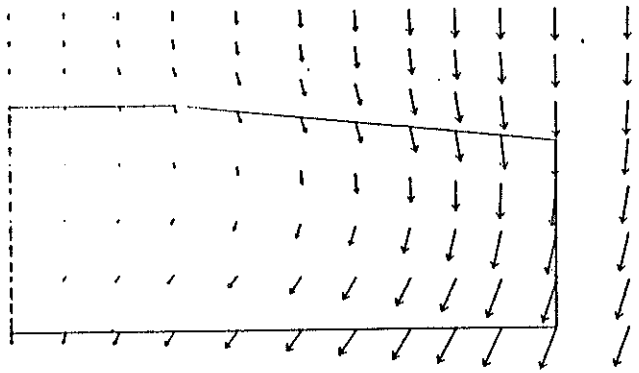

Fig. 15

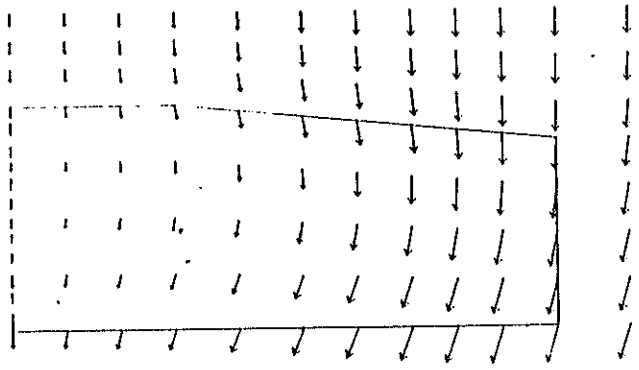

Fig. 16

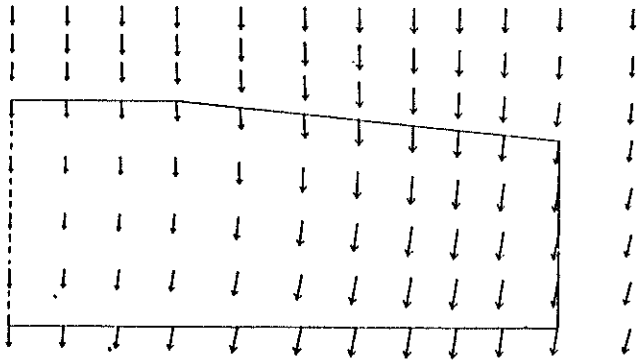

Fig. 17

LIST OF SYMBOLS

$\vec{B}$	vector of magnetic induction
$\vec{H}$	vector of magnetic field strength
$\vec{E}$	vector of electric field strength
μ	permeability
$\vec{J}$	vector of current density
σ	electrical conductivity
$\vec{A}$	magnetic vector potential
φ	electrical potential
∇	Nabla operator
∇^2	Laplace operator
θ	angle of cylindrical coordinates
r	radial distance in cylindrical coordinates
x,y,z	carthesian coordinates
F	functional
$L, \bar{L}, D$	linear operators
v, u	arbitrary variable
v^*	complex conjugate of v
ρ	load
ω	periodicity
$\vec{n}$	normal unit vector on boundary surface
$\vec{i}, \vec{j}, \vec{k}, \vec{s}$	unit vectors
t	time
$\{\ \}$	column vector
$[\ ]$	matrix
$[\ ]^T$	transposed matrix
$[N]$	matrix of shape functions
$[K]$	stiffness matrix
$[M]$	mass matrix
$\{P\}$	load vector
X^K	K^{th} symmetric component
T_{vx}, T_{xv}	transformation matrices

REFERENCES

[1] Norrie, D.H., de Vries, G., The Finite Element Method (Fundamentals and Applications). Academic Press, New York, 1973.

[2] Mikhlin, S.G., The problem of the minimum of a quadratic functional. Holden Day, 1965, San Francisco.

[3] Harink, T.G.M., Berekening van Magnetische Velden met behulp van de Eindige Elementen Methode. Doctoraalverslag Technical University Twente, Dept. of Applied Mathematics.

[4] Zienkiewicz, O.C., The Finite Element Method in Engineering Science. McGraw-Hill.

[5] McCormick, C.W., MSC/NASTRAN User's Manual. The Macneal-Schwendler Corp., Los Angeles, 1978 rev. ed.

[6] Joseph, J.A., MSC/NASTRAN Application Manual. The Macneal-Schwendler Corp., Los Angeles, 1977.

[7] Fortescue, C.L., Method of symmetrical co-ordinates applied to the solution of polyphase networks. AIEE 1918 (presented at the 34th Annual Convention of the American Institute of Electrical Engineers, Atlantic City, N.J., June 28, 1918).

BENDING MOMENTS COMPUTATION IN SUPERCONDUCTING TOROIDAL COILS OF DIFFERENT SHAPES, FOR TOKAMAK FUSION EXPERIMENTS, IN NORMAL AND FAULTY CONDITIONS

M.V. Ricci, M. Caciotta[+] and F. Nesci[x]
C.N.E.N., Laboratorio Superconduttività, Centro di Frascati, Rome, Italy

ABSTRACT

The determination of the bending moments distributions for toroidal coils of different shapes, when a coil goes normal, helps the choice of the shape that requires the lightest mechanical structure.

1. INTRODUCTION

One of the main problems presented by Tokamak fusion reactors is the behaviour of the superconducting toroidal coils in fault conditions, i.e. when one of them collapses to the normal state.
In principle the coils can be operated in two different ways: either connected to constant current generators, or short circuited once energized. In the first case, if one coil collapses, a very high voltage develops at the generators, but the current remains constant. In the second case, large extracurrents develop in the neighbouring coils. These extracurrents interact with the modified magnetic field pattern and produce large variations of the bending moments acting on the windings. With constant current generators this effect is limited to the modification of the field pattern. The large voltages that tend to develop in the first case can be limited by an electronic system. The large moments of the second solution require an external mechanical structure.
Certainly none of these two extreme solutions will be adopted because the large voltages would damage the coils and the current generators, while large extracurrents would produce a collapse of the whole superconducting system. The final solution will try to eliminate these problems but it is unlikely that extracurrents will be completely avoided.
In this work we consider the coils short-circuited with no limitation to the extracurrents. It is clear that in this way we obtain overestimated values of forces, which must be considered as limit values.Most of the designs of toroidal systems consider D-shaped coils which, in normal conditions, are only tensioned.

+) Istituto Elettrotecnico, Università di Roma

x) Candidate for degree of Istituto Elettrotecnico, Università di Roma.

The structure, which is required to substain the stresses in fault conditions, is inactive for most of the life of the reactor.
The aim of this work is to analyze the possibility that, by adopting a different shape for the coils, the structure can be lighter.
This may happen if the stresses that are generated in fault conditions compensate, at least partially, those already acting during normal operation.
The bending moments distribution changes, but the absolute values can be smaller than in the case of D-shaped coils.

2. COMPUTATION PROCEDURES

As a model of D-shaped coils, we consider those of the FINTOR design[1].
Each layer of conductor has its own pure tension D-shape. This causes a strong increase of the cross-section of the coils in the upper (and lower) part [2].
For computing requirements, the real shape has been simulated by four sub-coils as shown in Fig. 1[3].
Then a circular shape has been considered such that the dimension of the reactor are the same (Fig. 2).
In this way also the magnetic field on the plasma region is the same.
To calculate the extracurrents, it is necessary to determine the mutual inductance coefficients, a problem which is complicated by the shape of the coils.
We have then developed the code INDA which utilizes three different principles[4]. The first is the summation principle, according to which the coefficient can be calculated as the sum of those between the real or fictitious parts in which the coils have been divided.
The second one is the sectioning principle, that allows a subdivision of the cross-section in smaller elements and to sum the coefficients of each element with respect to the others (fig. 3). The third principle is that of Rayleigh. If the dimensions of the elements are small, the coefficients can be calculated as a combination of those between filaments passing through the center and the corners of the elements (fig. 4).
Of course, the larger is the number of elements, the better is the approximation.
The forces acting on the different points of the windings have been computed using the local values of the field and of the current density [3].
The magnetic field pattern has been calculated using the three dimensional code MAG3D-WF [5].
The computation of the bending moments has been carried out as follows: [6] the orizontal plane of symmetry divides the coil in two halves which are considered as curved beams. Each beam is rested at one end while is hinged at the other end (fig. 5).

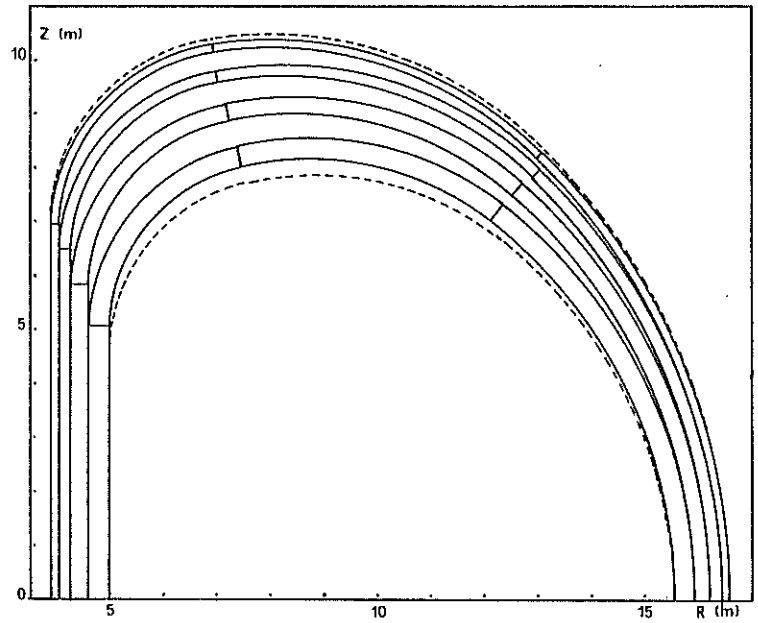

Fig. 1 - Sub-coils that approximate the FINTOR D-shaped coils.

The effect of one beam on the other is represend by a bending moment at the hinged end. More details on this code are reported in ref. 7.

3. RESULTS AND DISCUSSION

In Table I are reported, in percentages, the extra-currents for the D-shaped and circular coils produced by the failure of coil No. 1.
We can see that they assume a relevant value only for the nearmost coils (2 and 24). For force calculations we have then assumed that the current of the rest of the coils remain constant.
In Table II (and fig. 6) are reported the bending moments, on the plane of the coil, for the D-shaped coil No. 2, in normal and fault conditions.
In Table III (and fig. 7) are reported the results for the circular coils.

For the D-shaped coils, in normal conditions, the bending moments should be zero. The data of Table II give a maximum value on section No. 10 of about 1500 ton x m. This is probably due to the approximations used for the compu-

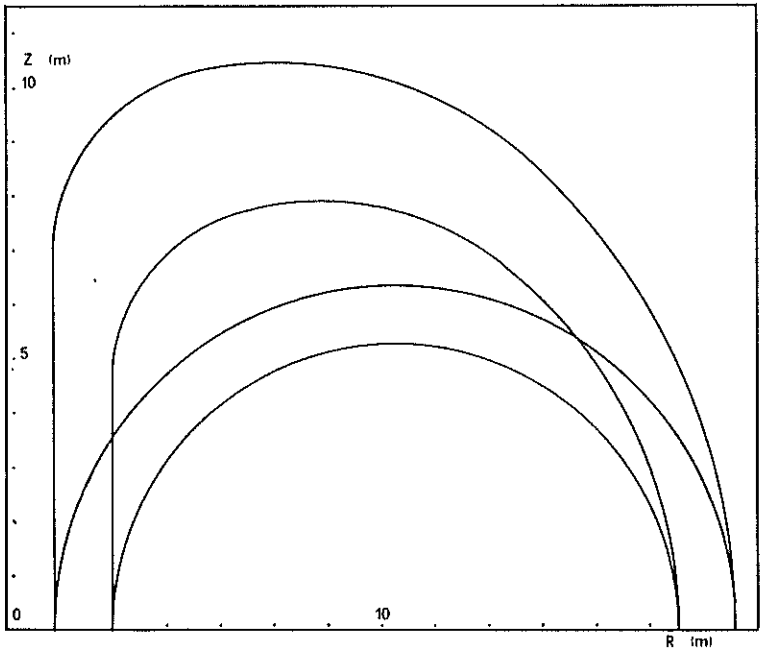

Fig. 2 - Compared dimensions of the circular and D-shaped coils.

Table I: Extra-currents in D-shaped and circular coils

Number coil	Circular collapsed	D-shaped collapsed
1		
2	39.0 %	42.0 %
3	-.9 %	-.1 %
4	.3 %	.1 %
5	.2 %	-.8 %
6	.2 %	3.2 %
7	.2 %	-.3 %
8	.1 %	2.8 %
9	-.1 %	-2.3 %
10	.2 %	1.4 %
11	.2 %	.4 %
12	-.3 %	.9 %
13	.4 %	.8 %

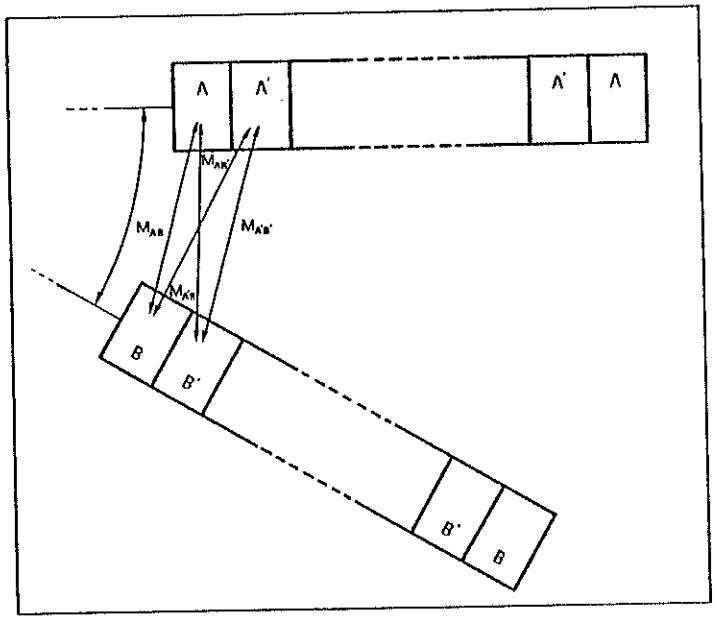

Fig. 3 - Sectioning principle: $M = M_{AB} + M_{A'B} + M_{AB'} + M_{A'B'}$

Table II: Bending moments in the more stressed D-shape coil in normal and fault conditions. The moments are measured in kton x m.

Section number	Normal	Fault
5	0.0	0.0
6	-.1	-.1
7	.3	.6
8	.9	1.3
9	1.3	2.0
10	1.5	2.3
11	1.5	2.2
12	1.2	1.7
13	.6	.9
14	.6	.8
15	.6	.7
16	.2	.1
17	-.3	-.5
18	-.2	-.3
19	0.0	0.0
20	0.0	0.0

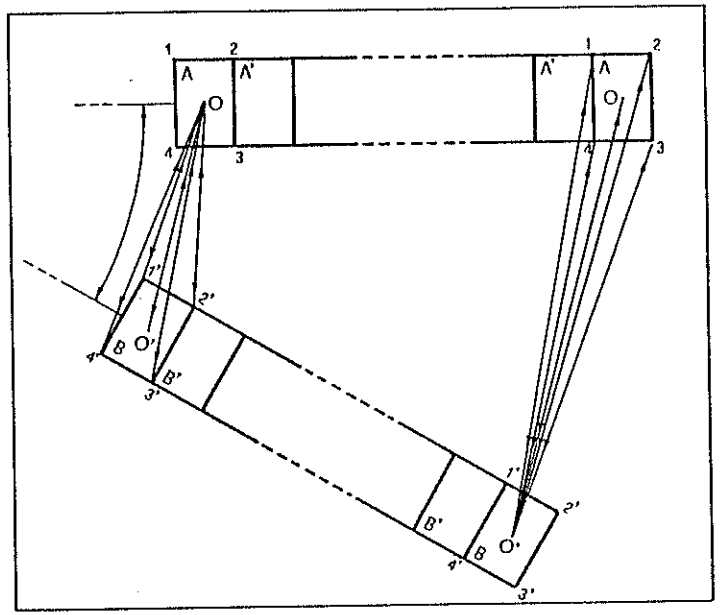

Fig. 4 - Rayleigh principle:
$M = 1/6\ (M_{o1'} + M_{o2'} + M_{o3'} + M_{o4'} + M_{o'1} + M_{o'2} + M_{o'3} + M_{o'4} - 2M_{oo'})$

ter calculations. However, we must consider that the bending moment on one section results from the sum of the forces acting on all the preceeding sections, which are of the order of 10^5 ton x m.
When one coil goes normal, the bending moments on the nearmost coils reach a maximum value of 2300 ton x m, which is not dramatically larger than that in a normal conditions. This result can be understood if we consider the fact that the failure of one coil, out of 24, produces a limited variation of the field pattern. As a consequence the pure tension shape is not much different.
As expected, the moments acting on the upper parts of the winding tend to reduce the height of the coil, while those on the external parts tend to enlarge it.

For the circular shape, large moments are present even in normal conditions and increase largely in fault conditions. The direction of the moments is opposite to the preceeding case.
These results confirm that an "intermediate" shape must exist , such that a reversal of the moment direction oc-

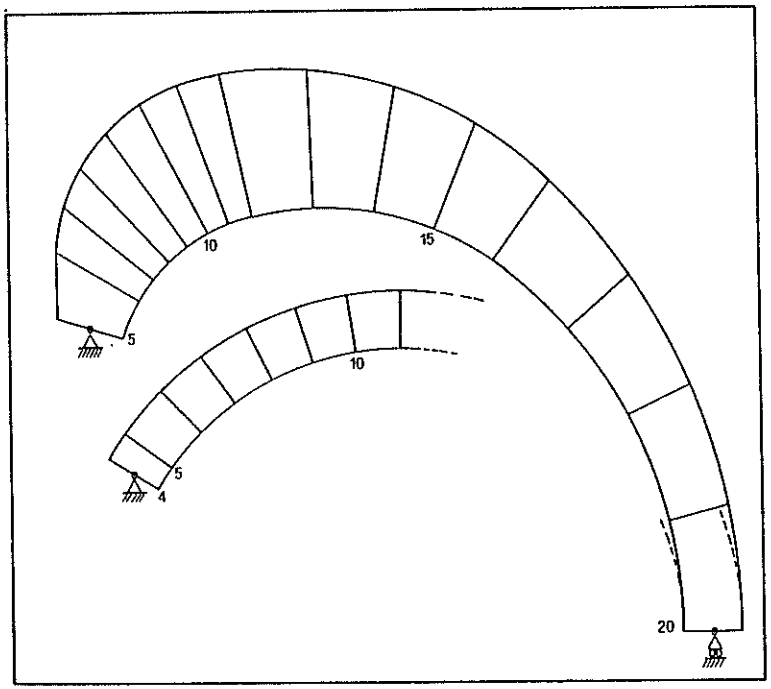

Fig. 5 - Mechanical representation of an half-coil. Positive moments are clockwise.

curs going from normal to faulty conditions.
The results indicate that this shape is close to the D that we have considered. In this case, the absolute values of the moments should be smaller than those that develop in faulty conditions for D-shaped coils.
Work is in progress to determine the exact shape of these coils.

REFERENCES

1. "FINTOR-1. A Minimum Size Tokamak DT Experimental Reactor", ed. Farfaletti-Casali, J.R.C. EURATOM, Ispra, 1977.

2. Pasotti, G. et al. "A Preliminary Study of the Superconducting Toroidal Magnet for FINTOR-1 Reactor", IEEE Trans.Magn. MAG-13, 1, 617 (1977).

3. Pasotti G. and Ricci M.V., "Forces Distribution in the D-shaped Coils of a Tokamak Reactor, in Normal and Fualt Conditions", presented to the X Symp. Magnet Technology, Padue (Italy), September 1978.

4. Grover, F.W. "Inductance Calculations", ed. Van Nostrand.

5. Ricci, M.V., "MAD3D-WF1, un codice per il calcolo del campo di sistemi magnetici tridimensionali", Report CNEN N. 77/22 (C.N.E.N., Centro di Frascati, 1977).

6. Timoshenko, S., "Resistence des materiaux", Librairie Polytechnique Ch. Beranger, 1947.

7. Caciotta, M., Sacerdoti, G., "Stresses Computation Produced by a Superconducting-Normal Single Coil Transition, in a Todoidal Magnet for Fusion Research Tokamak", proc.COMPUMAG Conference, Oxford, 1976.

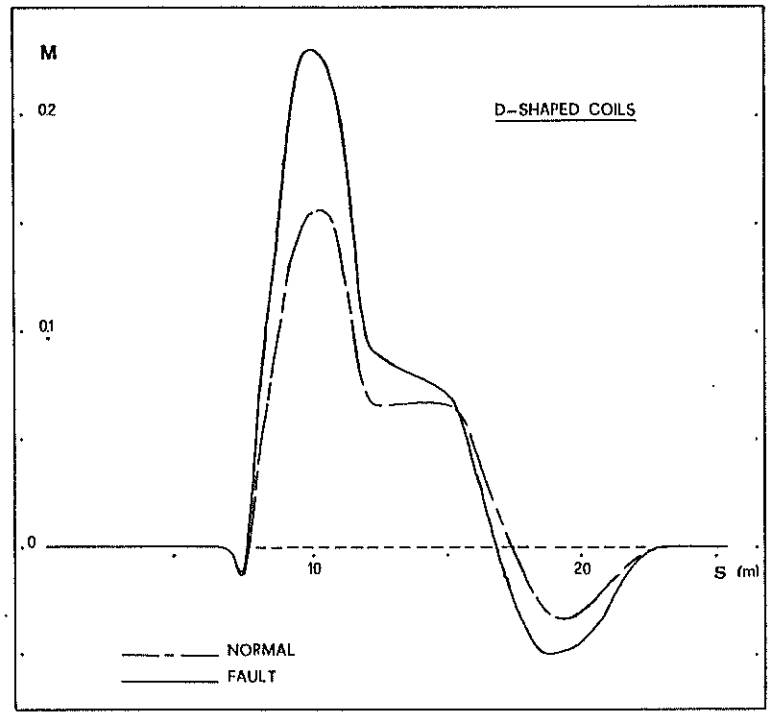

Fig. 6 - D-shaped coils: bending moments distribution (in ktons x m) in normal and fault conditions for the most stressed coils.

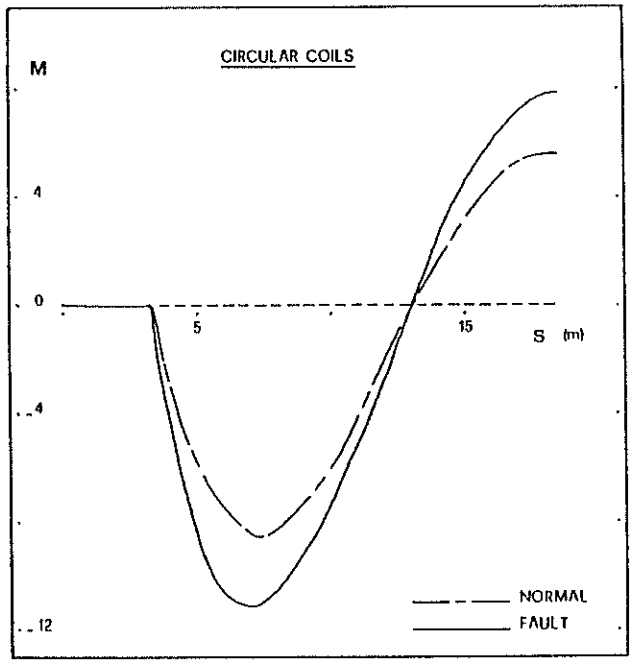

Fig. 7 - Circular coils:bending moments distribution in normal and in fault conditions in the most stressed coils.

Table III: Bending moments in the more stressed circular coil in normal and fault conditions. The moments are measured in kton x m.

Section number	Normal	Fault
4	0.0	0.0
5	-1.5	-2.8
6	-4.9	-7.2
7	-7.1	-10.0
8	-8.3	-11.3
9	-8.5	-11.5
10	-8.1	-10.8
11	-7.1	-9.4
12	-5.7	-7.5
13	-4.0	-5.2
14	-2.2	-2.8
15	-.4	-.4
16	1.3	1.9
17	2.8	3.9
18	4.0	5.6
19	4.9	6.8
20	5.5	7.5
21	5.7	7.7

ACKNOWLEDGEMENT

The authors want to thank Mr.G. Pasotti for many helpfull discussion and advices during this work.

HOMOGENEIZING SURFACE COILS FOR PRECISION MAGNETS

U. Czok, G. Moritz, and H. Wollnik
II. Physikalisches Institut der Universität, Giessen, Germany

ABSTRACT

Surface coils produced by etching techniques were used to improve the homogeneity of a magnet. This magnet is designed for high precision ion optics. The improvement in the calculated width of an ideally focused particle beam (α_o= 40 m rad) was better than 2Ø for a magnet with and without homogeneizing coils.

1. INTRODUCTION

Particle spectrometers often require magnets which combine high resolving power and high transmission, thus corresponding to a high "Q-Value"[1]. This is equivalent to postulating a large field area enclosed by the beam envelopes. However, in such large areas the field deviations inevitably become large, which in turn cause a broadening of the image[2]. To avoid such image distortions the distribution of the magnetic flux density must be required to deviate only slightly from the design.

The authors will present a simple method to improve the homogeneity of the magnetic flux density in a large area magnet by using very thin coils at the pole faces. The improvement in resolving power due to the homogeneizing procedures is calculated by ray tracing methods. The advantage of the method is its simplicity, its small space consumption (coil thickness less than 0,1 mm) and, last but not least, its low price. Perhaps even more important, however, is its wide operating range at different flux densities.

2. REAL FLUX DENSITY DISTRIBUTION

In a window frame magnet (see Fig.1) with pole face

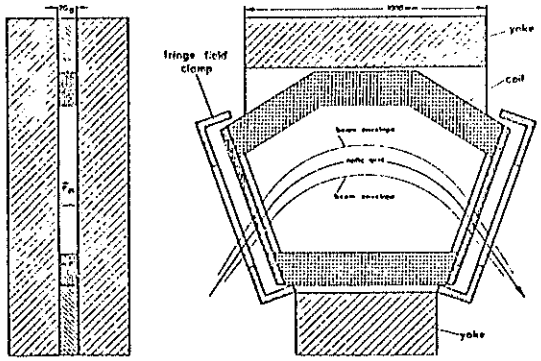

Fig. 1: A window frame magnet to be used for high precision ion optics. The beam envelopes are marked for a bundle of ions passing through the magnet. In the gap, 2Go=76mm, close to the pole faces two surface coils are mounted in order to homogenize the magnetic flux density.

areas of $0.4m^2$ the magnetic flux density distribution was measured by an NMR probe with an accuracy of a few times 10^{-6}. For this purpose the magnetic power supply was stabilized by another NMR probe achieving a stability of the magnetic flux density of better than $\pm 10^{-6}$ over 24 hours. With the first NMR probe the magnetic flux density was measured as close as possible both to the upper and the lower pole faces. In our case these minimal distances were 3mm, determined by the size of the NMR probe. From these measurements the flux density distribution in the midplane between the pole faces was calculated by a computer program[3]. This procedure yielded a higher precision for given errors of the measuring device than one could have obtained by measuring the flux density distribution in the midplane directly. This is because, as $\nabla^2 B$ vanishes in a volume, the largest variations of the magnetic flux density B are located on the surface.

In fig.2 the measured distributions close to the upper pole faces are plotted. The distribution close to the lower pole face is similar. The general shape of the magnetic flux density distribution in a normal dipole magnet is a saddle surface. The magnitude of the magnetic flux density is low near the entrance and exit boundaries of the magnet (fig. 3) since at these points the fringing field uses a certain portion of the main flux. Near the yokes of the magnet the magnetic flux density increases since a slightly larger than normal portion of the flux passes through a unit area of the pole faces.

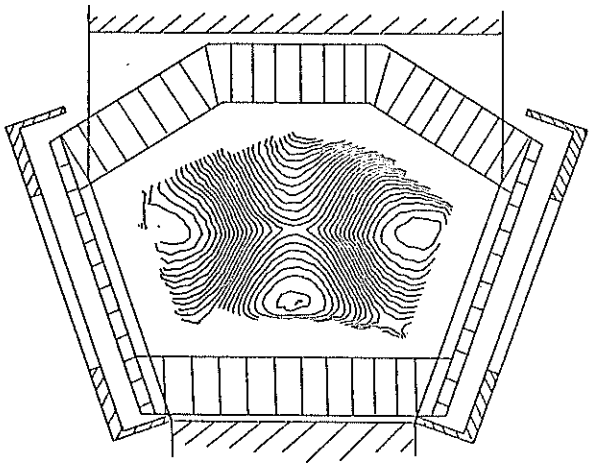

Fig. 2: The magnetic flux density distribution measured near the upper poleshoes. Lines of equal flux density are shown. The difference between neighbouring lines is $2 \cdot 10^{-5}$ T at an average flux density of 0.26 T

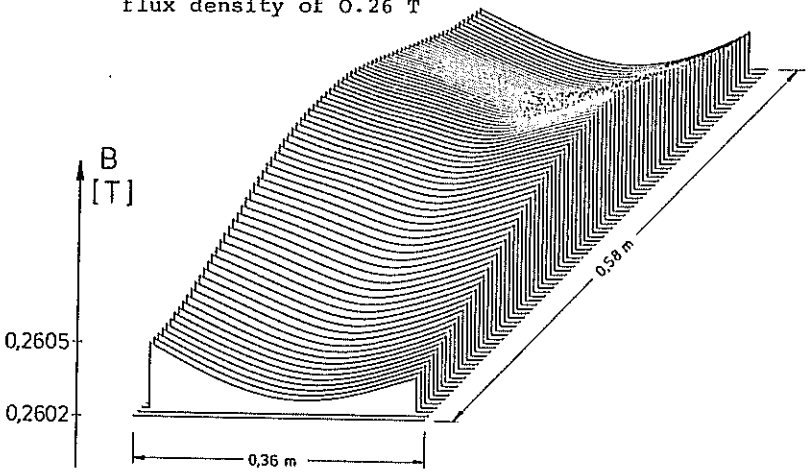

Fig. 3: The magnetic flux density in the midplane between the pole faces as calculated from measurements near the pole faces.
The deviations from an ideally homogeneous magnet are shown

3. HOMOGENIZING PROCEDURE

To compensate the inhomogeneity of the magnet one could try to scrape some iron off the pole faces in all areas where the magnetic flux density is too high, or add some iron foils in all those areas where it is too low. This procedure has been used successfully for NMR and for precision sector magnets[4]. A quite different proceudre uses surface currents[5]. Coils are used, designed that the magnetic potential of each coil will be an orthogonal function to the functions of the other coils. Thus the operator is able to optimize the currents in each coil without disturbing the effect of the other coils. These coils may be produced with wires or "printed" like electronic circuit boards.

We combined the shimming method with surface coils. The idea was to compensate the field deviations in those areas where the flux density deviations will occur. For this reason the surface coils add flux where the flux density is too small and substract flux, where the flux density is too high.
At each point of such a coil a current density $\vec{i}$ may be calculated according to the tangential component $\vec{B}_t$ of the mangetic flux density $\vec{B}$ which must be compensated. In order to determine the current which must be passed through such a coil we must determine the tangential component B_t of the magnetic flux density $\vec{B}$ in the plane of the pole faces. Homogenizing B_n (i.e. making $\partial B_n/\partial t=0$) is equivalent to making $\partial B_t/\partial n=0$ due to Maxwell's equation curl $\vec{B}=0$. Naturally this postulate is fulfilled if we require $B_t=0$. This can be achieved by having a surface current I flow in the pole face perpendicular to B_t. For this purpose consider a cross sectional view of the pole face perpendicular to the plane shown in fig. 2 in the direction $\vec{t}$ of the tangential component B_t as indicated in fig. 4.

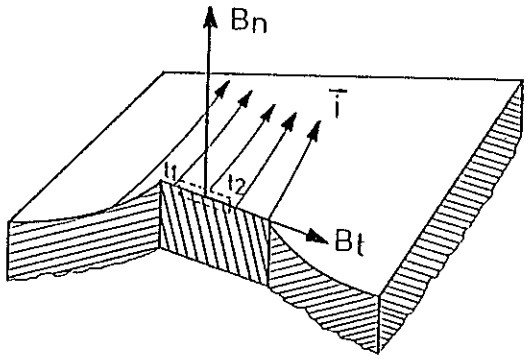

Fig. 4: A current density $\vec{i}$ on a iron surface produces a magnetic flux density distribution $\vec{B}$ with a component B_n perpendicular to the surface and a component B_t in the surface perpendicular to the current direction.

The B_t compensating current can now be determed:

$$I = \oint \vec{H}\,d\vec{s} = \int_{t_1}^{t_2} (B_t/\mu_0)\,dt \qquad (1)$$

by integrating along the dashed line in fig.4. Note that the part for which $\mu>10^3$ is neglected.

Next consider the tangential component B_t.

An NMR probe, used for high precision magnetic field measurements, can not be used to measure B_t directly since only the total magnetic flux density $|\vec{B}| = B = \sqrt{B_t^2 + B_n^2}$ is measured. Since the magnitude of B_t, in most cases is very small compared to the normal component B_n one can write:

$$B = B_n \left[1 + 0.5 \left(B_t/B_n\right)^2 + \ldots\right] \approx B_n \qquad (1)$$

Assuming that the direction of B_t is parallel to the direction of the gradient of B_n, the current I must flow in the direction of lines of equal flux density in fig. 2. Furthermore if B_t varies linearly across the magnet gap $2G_o$ and B_t vanishes in the midplane because of symmetry, i.e. $B_t/G_o \approx \partial B_t/\partial n$ then we may estimate:

$$B_t \approx G_o \frac{\partial B_t}{\partial n} = G_o \frac{\partial B_n}{\partial t} \approx G_o \frac{\partial B}{\partial t} \qquad (3)$$

Experience indicates that these rough estimates are sufficient for all investigated cases.
Combining B_t from eq.(3) with eq.(1) the compensating current I that must pass between the lines of magnetic flux B_2 and B_1 perpendicular to the gradient of B can be written as:

$$I \approx \frac{G_o}{\mu_o} \int_{t_1}^{t_2} \frac{\partial B}{\partial t}\, dt = \frac{G_o}{\mu_o} \left[B(t_2) - B(t_1)\right] = \frac{G_o}{\mu_o}\left(B_2 - B_1\right) = \frac{G_o}{\mu_o} \Delta B \qquad (4)$$

The ΔB between two neighbouring lines of equal magnetic flux density is constant throughout fig. 2. Thus the tangential component B_t should be able to be compensated everywhere on a pole face if the same current I, determined according to eq. (4), is passed through all lines of equal flux density.

This condition can be achieved by producing two etched circuit boards which have copper stripes of the same shape as the lines of equal flux density in fig. 2 and passing through all these copper stripes the same current I. On these etched circuit boards all lines of equal flux density are advantageously closed outside of the region which is to be homogenized, that is the region in which the particles will move. This is accomplished by surrounding the field distribution with a distribution which is continuous to the measured region and has a constant value outside. (fig. 5,6)

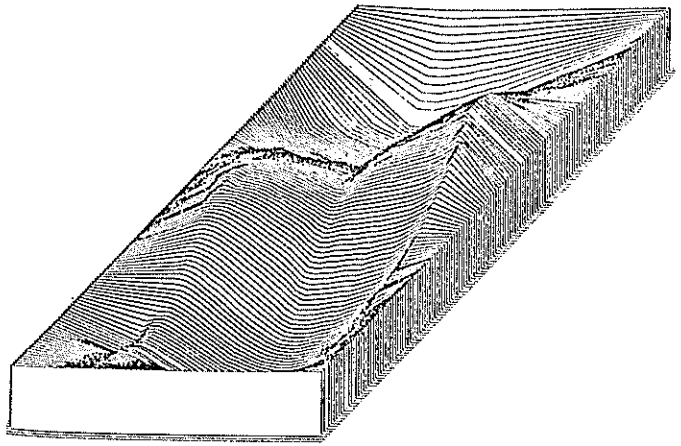

Fig. 5: The field distribution surrounded with values which are all equal at the outer boarder and are continuous to the measured values

The connection of the different loops of copper stripes

is made so that the current flows on one side of the printed circuit board in a kind of spiral from the outside to the points of highest or lowest flux densities (see fig. 7).

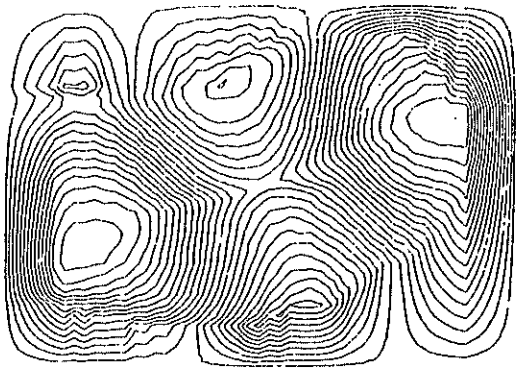

Fig. 6: The lines of constant flux density are closed by the surrounding values

At these points the current passes through to the other side of the etched circuit board where again a copper lead spirals outward. This spiral is complementary to the upper side thus filling all remaining gaps in the upper side. The currents on the two sides always flow in the same direction. This double etched circuit board ensures that the current density is almost continuous.

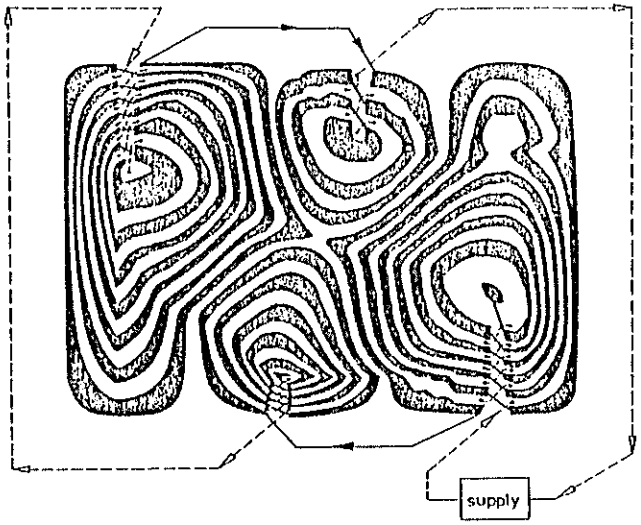

Fig. 7: The area between two neighbouring lines of constant flux density are painted black, and the interconnections between two windings are inserted. The connections on the back are marked by a dashed line.

After the coils, which closely represent the flux density distributions of fig. 2, had been placed at the corresponding pole faces a current I was passed through them according to eq.(1). By measuring the flux density distribution $B(x,y,z=const)$ both with and without a current in the circuit boards, and by calculating

$$V(I) = \sum_{n=0}^{N} \left[B(I, x_n, y_n, z_n) - B_0(I) \right]^2$$ for different currents,

the current which minimizes V(I) was found. Here $B_o(I)$ is the average flux density

$B_o(I) = \frac{1}{N} \sum_{n=0}^{N} B(I, x_n, y_n, z_n)$. The deviation between this optimal current and the value found from eq.(4) was only 4 %. This deviation should be acceptable for most cases. Thus the estimates of eqs.(1-3) seem sufficient. The resultant overall flux density distribution has also been recorded near the upper and lower pole faces by an NMR (fig. 8).

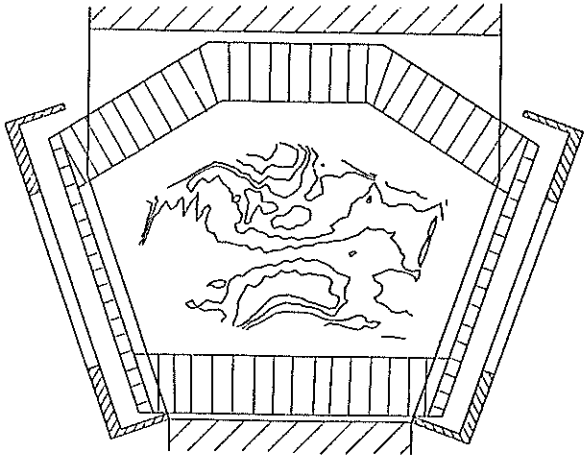

Fig. 8: The magnetic flux density, corrected with homogeneizing-coils, measured near the upper poleshoe.

Note that in Figure 9 the saddle shaped distribution

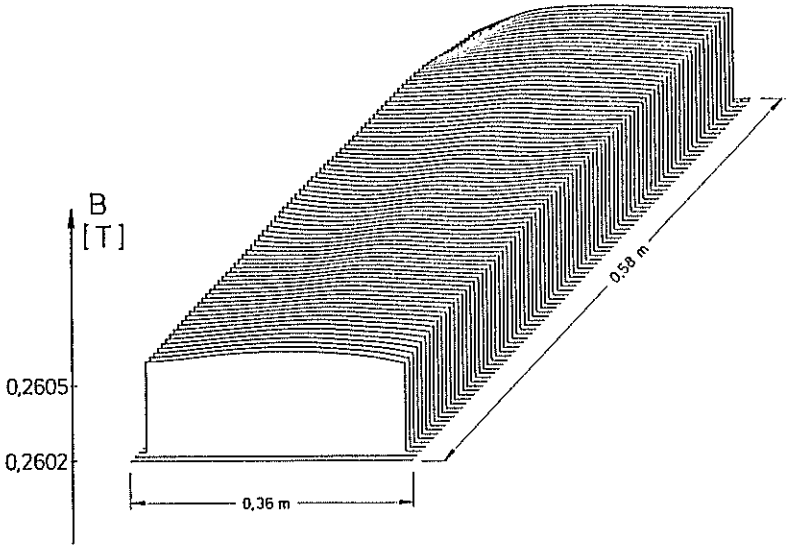

Fig. 9: The flux density in the midplane as calculated from the measurements close to the pole faces after the homogenizing.

of fig. 3 has disappeared completely and the remaining inhomogeneities are less than 10 % of the original ones.

To show the effect of this homogenizing procedure for a mass spectrometer or separator we have calculated how a bundle of charged particles originating from a point source would be deflected in the midplane with the currents I=0 and the optimal current I=145mA (e.g. $I = G_o \cdot \Delta B / \mu_o = 151 mA$ in our case for $\Delta B = 5 \cdot 10^{-6} T$, $2G_o = 76 mm$ and $\mu_o = 4 \cdot 10^{-7} Vsec\ A^{-1} m^{-1}$).

The divergence of the particle beam, used for the ray tracing procedure, was $\alpha_0 = 40$ mrad. The deviations of the different trajectories in the real magnetic field (see fig. 3) from the trajectories in an ideally homogeneous magnetic field are plotted in fig. 10.

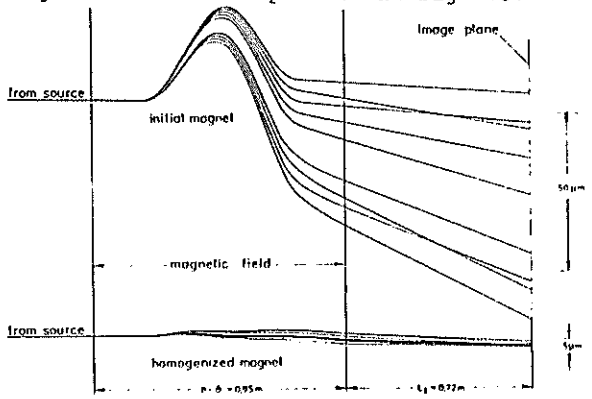

Fig. 10: The deviations of particle trajectories for a real magnetic sector field from an ideal homogeneous sector field are demonstrated (the radius of the optic axis is 0.5 m and the angle of deflection 109°). It is assumed that the particles originate from a point source. The different lines indicate characteristic trajectories within the ion bundle. Obviously there are no deviations until the magnet entrance boundary. The deviations become very large in the magnet and are still significant at the image. In the upper part of the graph the deviations of the particle trajectories in the initial real magnetic field (see fig. 2 and 3) are shown and in the lower part the deviations in the field homogenized by surface coils (see fig.8 and 9).

In this case the minimal width of the image of the point source should be about 70 μm if all image aberrations are corrected. The same type of plot was made for a magnet homogenized with the described surface coils. The image size here was found to be only about 2.5 μm. In each case the same initial bundle of particles was assumed.

4. HOMOGENIZING AT DIFFERENT FLUX DENSITIES

The described homogenizing procedure using surface currents seems very effective. Although we have described its action here only for a given magnetic flux density (0.26 T), we have also varied the flux density from 0.2 T to 0.4 T. As expected it was observed that mainly the height but not the shape of the flux density distribution varied with the flux density. Thus the homogenizing procedure with surface coils showed almost equally good results for different flux densities. The current in the correction coils, however, had to be varied according to eq.(4) which, it should be noted, does not increase linearly with B. Thus the use of surface coils should be superior to the usual method of homogenizing, the shimming (i.e. adding or removing thin sheets of iron from the pole faces), since in this case all corrections automatically do increase linearly with the magnetic flux density.

At very high flux densities we expect a reduced homogeneity through the use of surface coils since the shape of the flux density distribution should vary due

to saturation effects. In this case, however, one can extend the homogenizing procedure by using two sets of homogenizing coils for the two different flux densities B_1 and B_2.
The homogenizing currents at the flux density B_1 would be I_1 in the first set of coils and I_2 in the second set of coils for B_2. For any flux density B in between, the current in the first of the two coils then should be $\alpha_1 \cdot I_1$, and in the second $\alpha_2 \cdot I_2$ with properly chosen coefficients α_1, α_2. In a first order approximation these coefficients can be determined from:

$$\alpha_1 = (B_2 - B)/(B_2 - B_1) \qquad \alpha_2 = (B - B_1)/(B_2 - B_1)$$

5. SUMMARY

The described procedure to use surface coils for improving the homogeneity of a given dipole magnet has been shown to diminish the original deviations in magnetic flux density by more than a factor of ten.
The ion optical resolving power of a sector magnet corrected for image aberrations should increase even more than this factor.
The method is imple and straightforward. It can be applied to any existing magnet whether its initial homogeneity is good, fair, or only reasonable.

6. ACKNOWLEDGEMENTS

The authors are grateful for valuable discussions with D. Crombach. We would also like to thank the "Deutsche Forschungsgemeinschaft" for financial support.

7. REFERENCES

1 H. Wollnik, Nucl. Instr. and Meth. 95 (1971) 453.

2 T. Joy and N.R.S.Tait, Nucl. Instr. and Meth. 127 (1975) 485

3 H. Wind, Nucl. Instr. and Meth. 84 (1970) 117

4 SIN, Newsletter No. 5 (ETHZ-SIN R-71-0), SIN, Switzerland

5 Several Patents, i.e. U.S. Patent 348.442
W.A. Anderson, Review of Scient. Instr. March 1961, 241 - 250